



저작자표시-비영리-변경금지 2.0 대한민국

이용자는 아래의 조건을 따르는 경우에 한하여 자유롭게

- 이 저작물을 복제, 배포, 전송, 전시, 공연 및 방송할 수 있습니다.

다음과 같은 조건을 따라야 합니다:



저작자표시. 귀하는 원저작자를 표시하여야 합니다.



비영리. 귀하는 이 저작물을 영리 목적으로 이용할 수 없습니다.



변경금지. 귀하는 이 저작물을 개작, 변형 또는 가공할 수 없습니다.

- 귀하는, 이 저작물의 재이용이나 배포의 경우, 이 저작물에 적용된 이용허락조건을 명확하게 나타내어야 합니다.
- 저작권자로부터 별도의 허가를 받으면 이러한 조건들은 적용되지 않습니다.

저작권법에 따른 이용자의 권리는 위의 내용에 의하여 영향을 받지 않습니다.

이것은 [이용허락규약\(Legal Code\)](#)을 이해하기 쉽게 요약한 것입니다.

[Disclaimer](#)

이학박사학위논문

Topological Phases in (111)-oriented
BaBiO₃-bilayer Heterostructures

(111)-방향 BaBiO₃ 겹층 이질구조에서
구현되는 위상학적 상

2016년 2월

서울대학교 대학원

물리천문학부

김 록 연

Topological Phases in (111)-oriented
BaBiO₃-bilayer Heterostructures

(111)-방향 BaBiO₃ 겹층 이질구조에서
구현되는 위상학적 상

지도교수 유재준

이 논문을 이학박사 학위논문으로 제출함

2016년 2월

서울대학교 대학원

물리천문학부

김 록 연

김록연의 이학박사 학위논문을 인준함

2015년 12월

위원장 김기훈 (인)

부위원장 유재준 (인)

위원 임지순 (인)

위원 노태원 (인)

위원 진호섭 (인)

**Topological Phases in (111)-oriented
BaBiO₃-bilayer Heterostructures**

Rokyeon Kim

Supervised by
Professor **Jaejun Yu**

A Dissertation
Submitted to the Faculty of
Seoul National University
in Partial Fulfillment of
the Requirements for the Degree of
Doctor of Philosophy

December 2015

Department of Physics and Astronomy
Graduate School
Seoul National University

Abstract

Graphene—a representative two dimensional (2D) system whose low-energy electrons are described by the massless Dirac fermion—has been drawn great attention, and it triggered the outburst of 2D materials research. Among various capable applications, graphene was suggested as a platform for topological electronics; following the quantum spin Hall (QSH) phase pioneered by Kane and Mele, diverse topological phases have been introduced in graphene via generating the mass-gap at the Dirac point. For example, graphene can host the QSH phase through the gap-opening induced by the spin-orbit coupling (SOC), the quantum valley Hall (QVH) phase by the inversion symmetry breaking, and the quantum anomalous Hall (QAH) phase by the time-reversal symmetry breaking, respectively. To be more optimal for topological electronics applications, however, the large SOC and the bandgap tunability are necessary, which are hardly accessible in graphene.

In an attempt to find practical candidates, we suggest that the (111)-oriented BaBiO₃-bilayer (BBL) sandwiched by large gap perovskite oxides can provide an ideal platform for topological electronics. The low energy electronic structure of the (111) BaBiO₃-bilayer heterostructure is simply governed by the half-filled Bi 6*s*-orbital forming a buckled honeycomb lattice, which results

in the s -orbital Dirac fermions. The strong hybridization between the neighboring Bi- $6s$ and Bi- $6p$ orbitals enables the large SOC in the s -orbital band system. Finally, the abundant order parameters of oxide perovskite materials could break the symmetry in this oxide heterostructure, and open a gap at the Dirac point, which possibly leads to the engineering of the multiple topological phases.

The s -orbital Dirac fermion and its various topological phases in the (111) BBL heterostructure emerge from the confluence of three research areas in condensed matter physics: Dirac materials, oxide heterostructures, and topological electronics. It brings the graphene-like electronic structure in the oxide system, modifies and controls the bandgap at the Dirac point, and realizes the versatile topological phases. By taking account of the charge, spin, valley and pseudospin degrees of freedom of the Dirac fermion and the various quantum states of the oxide perovskites, we may find a zoo of topological quantum matters in this combined research area.

Our main results are summarized as follows: We present, based on first-principles calculations combined with the tight-binding analysis, that the perovskite heterostructure of BBL grown along the (111) direction can host QSH and QVH phases with appropriate choices of neighboring layers. When the same materials in the top and bottom layers sandwich the BBL, the s -orbital Dirac cone is emerging within the bandgap of sandwich layers. Due to the large spin-orbit coupling of the Bi atom and s - p hybridization, the Dirac cone that mainly consists of Bi s -orbital could opens a sizable non-trivial gap which turns the system into the QSH phase. For an asymmetric configuration, where the top and bottom layers are different, QVH phase with spin-valley coupling arises

as a result of the inversion symmetry breaking. In addition, we suggest a ferroelectric control of topological phases in $\text{BaTiO}_3/\text{BBL}/\text{BaTiO}_3$ heterostructure where the QSH and QVH phases can be selected via switching the polarization directions of BaTiO_3 layer. The (111) BBL heterostructure is proposed to be a feasible platform for spintronics and valleytronics as well as for topological engineering of the two-dimensional electron system.

Keywords: BaBiO_3 , heterostructure, honeycomb lattice, quantum spin Hall, quantum valley Hall

Student Number: 2008-20420

Contents

Abstract	vii
1 Introduction	1
2 Computational methods	6
2.1 Density functional theory	7
2.1.1 Hohenberg-Kohn theorem	7
2.1.2 Kohn-Sham approach	10
2.1.3 Exchange-correlation functional	11
2.1.4 Local density approximation	12
2.1.5 Generalized gradient approximation	13
2.2 Maximally localized Wannier function	14
2.3 Computational details	16
3 Topological phases in honeycomb system	19
3.1 Honeycomb system	20
3.1.1 Planar structure	20
3.1.2 Buckled structure	23

3.1.3	Dirac mass terms	26
3.2	Topological phases	28
3.2.1	Chern numbers	28
3.2.2	Classification of topological insulators	30
4	Electronic structures of BBL heterostructures	33
4.1	(111)-oriented BaBiO ₃ heterostructure	34
4.2	Emergence of a <i>s</i> -orbital Dirac cone	36
4.3	Symmetric configuration:	
	Quantum spin Hall insulator	37
4.4	Asymmetric configuration:	
	Quantum valley Hall insulator	42
4.5	Ferroelectric control of the topological phases	46
5	Tight-binding theory of (111)-oriented BaBiO₃-bilayer heterostructure	50
5.1	Crystal system	51
5.2	Tight-binding hopping Hamiltonian	53
5.3	Tight-binding SOC Hamiltonian	55
5.4	Effective low-energy Hamiltonian	56
6	Discussion	63
6.1	Spin-orbit coupling in <i>s</i> -orbital Dirac cone	64
6.2	Charge-ordering instability at symmetric configuration	66
7	Summary and perspective	68

Bibliography	71
Abstract in Korean	78

List of Figures

1.1	The interesting physics of BBL heterostructure is emerging from confluence of three topics in condensed matter physics. (1) Dirac materials: the low-energy electronic structure of the system is described by the simple Dirac Hamiltonian. (2) Oxide heterostructures: taking advantage of state-of-the-art oxide fabrication techniques, the heterostructures provide versatile controllabilities to the system. (3) Topological electronics: spintronics and valleytronics making use of QSH and QVH phases are realized in (111)-oriented BBL heterostructure.	3
2.1	The crystal structure of $\text{BaXO}_3/\text{BBL}/\text{BaYO}_3$. 8 bottom layers of BaXO_3 , BaBiO_3 -bilayer, and 8 top layers of BaYO_3 are shown. Only X , Bi , and Y atoms are drawn for simplicity. BaBiO_3 -bilayer form a buckled honeycomb lattice consists of upper triangular sublattice colored by blue and lower triangular sublattice colored by red.	17

3.1	(a) Primitive lattice vectors \mathbf{a}_1 and \mathbf{a}_2 for direct lattice. Honeycomb lattice is consists of two triangular sublattices denoted by filled-circle A and open-circle B . (b) First Brillouin zone in momentum space with two inequivalent K and K' points. Primitive vectors \mathbf{b}_1 and \mathbf{b}_2 for reciprocal lattice is shown.	20
3.2	Low-energy band structure of tight-binding model. Six Dirac cones are located at the corners of the first Brillouin zone with the Fermi level touching gap closing points.	22
3.3	(a) Top view and (b) side view of the crystal structure of buckled honeycomb lattice. Two sublattices are distinguished by different colors. The buckling angle θ is defined in (b). The angle is exaggerated in (b) for silicene.	24
3.4	Chern numbers distributions for (a) QSH and (b) QVH phases.	31
4.1	(a) The schematic picture of $\text{BaXO}_3/\text{BaBiO}_3/\text{BaYO}_3$ along the (111) direction investigated in this study. (b) The (111)-oriented BBL form a buckled honeycomb lattice consisting of red and blue triangular sublattices. (c) 2D hexagonal Brillouin zone and high symmetry points. (d)-(g) Schematic band structures emerging from the (111)-oriented BBL heterostructures in terms of SOC and inversion symmetry.	34
4.2	Band structure of perovskite BaBiO_3 . Bi-6s band has a large bandwith and cross the Fermi level.	35

4.3	Band structure of BaZrO ₃ /BBL/BaZrO ₃ (a) with and (b) without the SOC. (a) Band structure shows a massless Dirac cone near the K point. The Dirac cone is decoupled from the sandwich layers bands. (b) SOC opens the gap at the K point by 79 meV.	37
4.4	Topologically protected edge states of BaZrO ₃ /BBL/BaZrO ₃ for (a) zigzag edge and (b) armchair edge. The strip geometry is constructed with hopping parameters obtained from Wannier function method. Both edges states cross the Fermi level odd times in the half Brillouin zone.	40
4.5	(a) Band structure of BaHfO ₃ /BBL/BaZrO ₃ . Trivial bandgap is 0.924 eV. Valence band is split by 29 meV and Conduction band is split by 103 meV due to the SOC. (b) Calculated Berry curvature are drawn with color code. Atomic units are used. Berry curvature at K and K' are exactly opposite, which confirms the QVH phase.	43
4.6	In- and out-of-plane spin-texture of BaHfO ₃ /BBL/BaZrO ₃ for (a) VBM-1 and (b) VBM. The in-plane spin-texture is represented by arrow and out-of-plane spin-texture is color coded. Chirality of in-plane spin-texture is the same for K and K' while the out-of-plane spin-texture is opposite. The overall spin-texture of VBM is exactly opposite to the that of VBM-1.	44

4.7	(a) The symmetric configuration of BaTiO ₃ /BBL/BaTiO ₃ . (b) The asymmetric configuration of BaTiO ₃ /BBL/BaTiO ₃ . (c) Band structure of symmetric configuration of BaTiO ₃ /BBL/BaTiO ₃ . SOC opens the bandgap by 108 meV. See the text for detailed procedure to obtain this band structure. (d) Band structure of asymmetric configuration BaTiO ₃ /BBL/BaTiO ₃ . Trivial bandgap is 1.17 eV. Conduction band and valence band is split by 192 meV and 56 meV, respectively	47
4.8	Double cell geometry as shown in (c) is used to calculate the band structure of symmetric configuration of BaTiO ₃ /BBL/BaTiO ₃ . The total band structure is projected on (a) upper BBL and (b) lower BBL. The projected bands are represented by red color. They correspond to band structures of two symmetric configurations shown in upper part and lower part of (c). (d) Electron potential energy along the (111) direction. Effect of polarization can be seen in potential gradient.	49
5.1	Crystal system used for the tight-binding model of BBL heterostructure.	51
6.1	The next-nearest-neighbor hopping process is illustrated. See the text for a detailed description.	65
6.2	The relation between the bandgap and the external electric field.	67

List of Tables

4.1	Lattice parameters and SOC gap at K for Ba-based system. . .	41
4.2	Lattice parameters and SOC gap at K for Sr-based system. . .	41
5.1	The energy integral in terms of two-center integrals.	54

Chapter 1

Introduction

Graphene is a representative two-dimensional system whose low-energy band structure is described by the massless Dirac fermion where the linear dispersion is resulting from the single orbital in monolayer honeycomb lattice. The Dirac cone on honeycomb lattice possesses various degrees of freedom; charge, valley, real spin and sublattice pseudo-spin. When these are properly adjusted, the system can host diverse topological phases, e.g. QSH [KM05], QVH [XYN07], and quantum anomalous Hall (QAH) [Hal88] phases. This finding triggered the researches of spintronics and valleytronics devices in the honeycomb systems, but the studies of graphene and silicene/germanene/stanene (Si/Ge/Sn monolayer isostructural to graphene) revealed that the small atomic SOC strengths of composing atoms in the systems makes it difficult to realize and make use of its topological phases. Moreover, considering the controllability of the topological phases, QSH to QVH phase transition is typically controlled by applying an external electric field, which is volatile.

Since Ref. [XZR⁺11] suggested that the perovskite (111) bilayer can be

regarded as a buckled honeycomb lattice and predicted topological insulator in transition metal oxide (TMO) (111) bilayer, there have been many theoretical studies in these structures. All materials considered so far, however, were TMO where the electron correlation and crystal splitting of d orbitals play the important role in realizing the various topological phases [OZN⁺14, FR14]. Although the TMO (111) bilayer system could provide rich physics regarding the electron correlation in d orbitals, it may hinder the simple and concise description of the honeycomb system as the case in graphene.

Experimentally, compared to the state-of-the-art fabrication technique for perovskite oxide in (001) direction, the fabrication of (111) perovskite heterostructure with atomic precision might be challenging because the surfaces of (111) direction is usually charged. The synthesis work in this direction, however, is actively progressing these days [GZS⁺12, LKC⁺14, MMK⁺12, MMD⁺14], and successful growth of perovskite structure along (111) was reported very recently [HMT15].

In this thesis, as an attempt to bring the large SOC and introduce attainable controllability to the degrees of freedom and thus the topological phases in honeycomb systems, we design (111)-oriented BBL heterostructures. As will be discussed throughout this thesis, the interesting physics emerging from this structure is the confluence of three important topics in today's condensed matter physics. (see Fig 1.1) (1) Dirac materials: the low-energy electronic structure of the system is described by the simplest Dirac Hamiltonian, the same form as the graphene, that can host various topological phases. (2) Oxide heterostructures: taking advantage of state-of-the-art oxide fabrication techniques, the heterostructures provide versatile controllabilities to the system. In par-

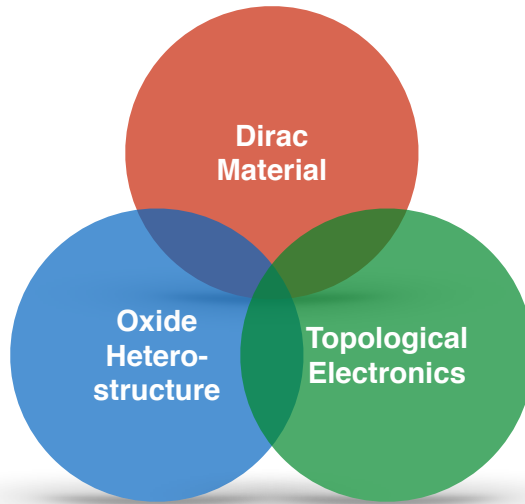


Figure 1.1: The interesting physics of BBL heterostructure is emerging from confluence of three topics in condensed matter physics. (1) Dirac materials: the low-energy electronic structure of the system is described by the simple Dirac Hamiltonian. (2) Oxide heterostructures: taking advantage of state-of-the-art oxide fabrication techniques, the heterostructures provide versatile controllabilities to the system. (3) Topological electronics: spintronics and valleytronics making use of QSH and QVH phases are realized in (111)-oriented BBL heterostructure.

ticular, the inversion symmetry can be turned on (off) by choosing the same (different) layers in top and bottom of BBO bilayer. (3) Topological electronics: spintronics and valleytronics making use of QSH and QVH phases are easily realized in BBL heterostructures, which make the (111)-oriented BBL as novel playground for the topological electronics.

This thesis is organized as follows:

Chapter 2 describes basic formalism of the density functional theory and maximally localized Wannier function method adopted in the study. Also, computational details for the calculation of BBL heterostructure is given.

In Chapter 3, we give an introduction to the general physics in a honeycomb system. Tight-binding model describing the single-orbital in the honeycomb lattice is studied with two representative examples, e.g. graphene and silicene. In particular, silicene, which has a buckled honeycomb lattice similar to BBL, is investigated in detail because the buckled structure and SOC allow us to control degrees of freedom. Topological phases realized in the honeycomb lattice is illustrated in general terms. Two topological phases, QSH and QVH phases, are given special focus.

Chapter 4 deals with first-principles calculation results of BBL heterostructure. The perovskite heterostructure of BBL grown along the (111) direction is shown to host QSH and QVH phases with appropriate choices of neighboring layers. In addition, we suggest a ferroelectric control of topological phases in $\text{BaTiO}_3/\text{BBL}/\text{BaTiO}_3$ heterostructure where the QSH and QVH phases can be selected via switching the polarization directions of BaTiO_3 layer.

Chapter 5 provide Slater-Koster [SK54] type tight-binding theory of BBL heterostructure. The low energy effective Hamiltonian for s -band is obtained

from the full tight-binding Hamiltonian by the down-folding method. From the effective Hamiltonian, we attempt to explain how the large SOC is possible in *s*-band system.

In Chapter 6, we discuss the results. We give a simple description of next-nearest-neighbor SOC process in BBL heterostructure. Also, we touch on the issue of charge-ordering instability of Bi atoms at symmetric configuration. Finally, various topological edge states that could be realized in the domain boundary of BBL heterostructures are discussed.

Chapter 7 concludes this thesis. We give summary and perspective of the study.

Chapter 2

Computational methods

This chapter describes basic formalism of the density functional theory (DFT) and local density approximation (LDA) and generalized gradient approximation (GGA) for exchange-correlations functionals. And maximally localized Wannier function method adopted in the study is briefly discribed. Also, computational details for the calculations of BBL heterostructures is given.

2.1 Density functional theory

The calculations of electronic structures provides qualitative understanding of physical properties of the materials in investigation. The density functional theory (DFT) is the first-principles calculation method for electronic structures in condensed matter physics. The formulation of DFT was initiated by P. Hohenberg and W. Kohn in their famous paper in 1964 [HK64]. These authors showed that a special role can be assigned to the density of electrons in the ground state of a quantum many-body system. The electron density, instead of a many-body wave function, is considered as a basic variable, i.e. that all properties of the system are functionals of the ground state density. This theorem have triggered widespread studies of DFT within Kohn-Sham approach. Local density approximation (LDA) and generalized gradient approximation (GGA) for exchange-correlation functionals are proven to be promising method for accurate, practical description of materials. In this section, we review the detailed formalism of DFT within LDA and GGA scheme.

2.1.1 Hohenberg-Kohn theorem

DFT is based on two theorems firstly proven by Hohenberg and Kohn [HK64]. These are stated and proved in the following.

Theorem 1. For any system of interacting particles in an external potential $V_{\text{ext}}(\mathbf{r})$, the potential $V_{\text{ext}}(\mathbf{r})$ is determined uniquely, except for a constant, by the ground state particle density $n_0(\mathbf{r})$.

Proof Suppose that there were two different external potentials $V_{\text{ext}}^{(1)}(\mathbf{r})$ and $V_{\text{ext}}^{(2)}(\mathbf{r})$ which differ by more than a constant and which lead to the same

ground state density $n(\mathbf{r})$. The two external potentials lead to two different hamiltonians, $\hat{H}^{(1)}$ and $\hat{H}^{(2)}$, which have different ground state wavefunctions, $\Psi^{(1)}$ and $\Psi^{(2)}$, which are hypothesized to have the same ground state density $n_0(\mathbf{r})$. Since $\Psi^{(2)}$ is not the ground state of $\hat{H}^{(1)}$, it follows that

$$E^{(1)} = \langle \Psi^{(1)} | \hat{H}^{(1)} | \Psi^{(1)} \rangle < \langle \Psi^{(2)} | \hat{H}^{(1)} | \Psi^{(2)} \rangle. \quad (2.1)$$

The strict inequality follows if the ground state is non-degenerate, and the last term can be written

$$\begin{aligned} \langle \Psi^{(2)} | \hat{H}^{(1)} | \Psi^{(2)} \rangle &= \langle \Psi^{(2)} | \hat{H}^{(2)} | \Psi^{(2)} \rangle + \langle \Psi^{(2)} | \hat{H}^{(1)} - \hat{H}^{(2)} | \Psi^{(2)} \rangle \\ &= E^{(2)} + \int d^3r [V_{\text{ext}}^{(1)}(\mathbf{r}) - V_{\text{ext}}^{(2)}(\mathbf{r})] n_0(\mathbf{r}), \end{aligned} \quad (2.2)$$

so that

$$E^{(1)} < E^{(2)} + \int d^3r [V_{\text{ext}}^{(1)}(\mathbf{r}) - V_{\text{ext}}^{(2)}(\mathbf{r})] n_0(\mathbf{r}). \quad (2.3)$$

On the other hand if we consider $E^{(2)}$ in exactly the same way, we find the same equation with superscripts (1) and (2) interchanged,

$$E^{(2)} < E^{(1)} + \int d^3r [V_{\text{ext}}^{(2)}(\mathbf{r}) - V_{\text{ext}}^{(1)}(\mathbf{r})] n_0(\mathbf{r}). \quad (2.4)$$

By adding Eq.(2.3) and Eq.(2.4), we obtain

$$E^{(1)} + E^{(2)} < E^{(1)} + E^{(2)}. \quad (2.5)$$

There cannot be two different external potentials differing by more than a constant which give rise to the same non-degenerate ground state charge density. The density uniquely determines the external potential to within a constant.

Theorem 2. For a given $V_{\text{ext}}(\mathbf{r})$, the exact ground state energy of the system is the global minimum value of the energy functional $E[n]$ in terms of the density $n(\mathbf{r})$, and the density $n(\mathbf{r})$ that minimizes the functional is the exact ground state density $n_0(\mathbf{r})$.

Proof The following energy functional

$$E_{HK}[n] \equiv \int d^3r V_{\text{ext}}(\mathbf{r})n(\mathbf{r}) + F_{HK}[n], \quad (2.6)$$

where $F_{HK}[n] = T[n] + E_{\text{int}}[n]$,

and $F_{HK}[n]$ is the sum of kinetic and Coulomb interaction energy. Consider a system with the ground state density $n^{(1)}(\mathbf{r})$ corresponding to external potential $V_{\text{ext}}^{(1)}(\mathbf{r})$, then

$$E^{(1)} = E_{HK}[n^{(1)}] = \langle \Psi^{(1)} | \hat{H}^{(1)} | \Psi^{(1)} \rangle, \quad (2.7)$$

where $\Psi^{(1)}$ is the wavefunction of the ground state. Now consider a different density, say $n^{(2)}(\mathbf{r})$, which necessarily corresponds to a different wavefunction $\Psi^{(2)}$. It follows that the energy $E^{(2)}$ of this state is greater than $E^{(1)}$, since

$$E^{(1)} = \langle \Psi^{(1)} | \hat{H}^{(1)} | \Psi^{(1)} \rangle < \langle \Psi^{(2)} | \hat{H}^{(1)} | \Psi^{(2)} \rangle = E^{(2)}. \quad (2.8)$$

Thus the energy given by Eq. (2.6) in terms of the Hohenberg-Kohn functional evaluated for the correct ground state density $n_0(\mathbf{r})$ is indeed lower than the

value of this expression for any other density $n(\mathbf{r})$.

2.1.2 Kohn-Sham approach

The Kohn-Sham approach is to replace the interacting many-body system with a different *auxiliary system* that can be solved more easily. Kohn and Sham made an ansatz that the ground state density of the original interacting system is equal to that of some chosen non-interacting system. This leads to independent-particle equations, or Kohn-Sham equation, for the non-interacting system that can be exactly soluble provided that all the difficult many-body terms are incorporated into an exchange-correlation functional of the density. By solving the equations, one finds the ground state density and energy of the original interacting system with the accuracy limited only by the approximations made in the exchange-correlation functional.

There are two assumptions: (1) The exact ground state density can be represented by the ground state density of an auxiliary system of non-interacting particles. (2) The auxiliary Hamiltonian is chosen to have the usual kinetic operator and an effective local potential $V_{\text{ext}}^{\sigma}(\mathbf{r})$ acting on an electron of spin σ at point \mathbf{r} .

The Kohn-Sham approach to the full interacting many-body problem is to rewrite the Hohenberg-Kohn expression for the ground state energy functional

in the form

$$E_{KS} = T_s[n] + \int d\mathbf{r} V_{\text{ext}}(\mathbf{r})n(\mathbf{r}) + E_{\text{Hartree}}[n] + E_{II} + E_{\text{xc}}[n], \quad (2.9)$$

$$\text{where } T_s = \frac{1}{2} \sum_{\sigma} \sum_{i=1}^{N_{\sigma}} |\nabla \psi_i^{\sigma}|^2, \quad (2.10)$$

$$E_{\text{Hartree}}[n] = \frac{1}{2} \int d^3r d^3r' \frac{n(\mathbf{r})n(\mathbf{r}')}{|\mathbf{r} - \mathbf{r}'|}, \quad (2.11)$$

E_{II} is the interaction between the nuclei, and $E_{\text{xc}}[n]$ is the exchange correlation energy functional.

The minimization of the energy E_{KS} with respect to the density $n(\mathbf{r}, \sigma)$ gives rise to the solution of the Kohn-Sham auxiliary system for the ground state.

2.1.3 Exchange-correlation functional

In the Kohn-Sham approach, the energy functional is separated by the independent-particle kinetic energy, the long-range Hartree terms, and the remaining exchange-correlation functional $E_{\text{xc}}[n]$ which can reasonably be approximated as a local or nearly local functional of the density. The energy $E_{\text{xc}}[n]$ is determined by the “coupling constant integration formula”, where the electronic charge is varied from zero (the noninteracting case) to the actual value (1 in atomic units), with the added constraint that the density must be kept constant during this variation. Then all other terms remain constant and the change in energy is

given by

$$\begin{aligned}
E_{\text{xc}}[n] &= \int_0^{e^2} d\lambda \langle \Psi_\lambda | \frac{dV_{\text{int}}}{d\lambda} | \Psi_\lambda \rangle - E_{\text{Hartree}}[n] \\
&= \frac{1}{2} \int d^3r n(\mathbf{r}) \int d^3r' \frac{\bar{n}_{\text{xc}}(\mathbf{r}, \mathbf{r}')}{|\mathbf{r} - \mathbf{r}'|},
\end{aligned} \tag{2.12}$$

where $\bar{n}_{\text{xc}}(\mathbf{r}, \mathbf{r}')$ is the coupling-constant-averaged hole

$$\bar{n}_{\text{xc}}(\mathbf{r}, \mathbf{r}') = \int_0^1 d\lambda n_{\text{xc}}^\lambda(\mathbf{r} - \mathbf{r}'). \tag{2.13}$$

Here $n_{\text{xc}}(\mathbf{r}, \mathbf{r}')$ is the hole summed over parallel ($\sigma = \sigma'$) and antiparallel ($\sigma \neq \sigma'$) spins.

The exact exchange-correlation energy can be understood in terms of the potential energy due to the exchange-correlation hole averaged over the interaction from $e^2 = 0$ to $e^2 = 1$. For $e^2 = 0$ the wavefunction is just the independent-particle Kohn-Sham wavefunction. $E_{\text{xc}}[n]$ can be considered as an interpolation between the exchange-only and the full correlated energies at the given density $n(\mathbf{r}, \sigma)$.

2.1.4 Local density approximation

In the exact DFT formalism, the exchange-correlation energy functional is an unknown variable, so that the approximations are suggested such as local density approximation (LDA). In the slowly varying inhomogeneous electron system, $E_{\text{xc}}[n]$ can be written as

$$E_{\text{xc}}[n] \approx \int d\mathbf{r} n(\mathbf{r}) \epsilon_{\text{xc}}(n(\mathbf{r})) \tag{2.14}$$

where $\epsilon_{xc}(n(\mathbf{r}))$ is the single particle exchange-correlation energy of the homogeneous electron gas with density n . LDA assumes the slowly varying electron density in the real space and treats the inhomogeneous system as a piece-wise homogeneous one. Space is divided into a set of small discrete cells and the electron density in the volume ω_i is assumed to be constant. Then energy functional $G[n]$ is calculated by

$$G[n] \approx \sum_i \omega_i g^{homo}(n_i) \quad (2.15)$$

where $g^{homo}(n_i)$ is the energy density of an homogeneous electron system. Practically the correlation energy functional is constructed from fitting the quantum Monte Carlo simulation.

2.1.5 Generalized gradient approximation

For improvement over LDA, generalized gradient approximation (GGA) is introduced to consider the gradient of the density ∇n^σ as well as the value n at each point. The term GGA denotes a variety of ways proposed for functions that modify the behavior at large gradients in such a way as to preserve desired properties. It is convenient to define the functional as a generalized form of Eq. (2.14),

$$\begin{aligned} E_{xc}^{GGA}[n] &= \int d^3r n(\mathbf{r}) \epsilon_{xc}(n, |\nabla n|, \dots) \\ &\equiv \int d^3r n(\mathbf{r}) \epsilon_x^{homo}(n) F_{xc}(n, |\nabla n|, \dots) \end{aligned} \quad (2.16)$$

where F_{xc} is dimensionless and $\epsilon_x^{\text{homo}}(n)$ is the exchange energy of the unpolarized gas.

For exchange and correlations, the numerous forms for F_x are proposed by the Perdew and Wang (PW91) [PW92] and Perdew, Burke, and Ernzerhof (PBE) [PBE96], and that for F_c are determined by the Ma and Brueckner [MB68].

2.2 Maximally localized Wannier function

Electronic structure calculation typically adopt plane-wave basis set in solving the problem. The resulting wave functions, or Bloch functions $\psi_{n\mathbf{k}}$, are characterized by band index n and the crystal momentum \mathbf{k} . Alternatively, we may Fourier transform Bloch functions to obtain Wannier functions $w_{n\mathbf{R}}$ indexed by Bravais lattice vector \mathbf{R} instead of momentum \mathbf{k}

$$w_{n\mathbf{R}} = \frac{V}{(2\pi)^3} \int_{BZ} \left[\sum_m U_{mn}^{(\mathbf{k})} \psi_{m\mathbf{k}}(\mathbf{k}) \right] e^{-i\mathbf{k}\cdot\mathbf{R}} d\mathbf{k}, \quad (2.17)$$

where V is the unit cell volume, the integral is over the Brillouin zone, and $U_{mn}^{(\mathbf{k})}$ is a unitary matrix that mixes the Bloch states at each \mathbf{k} point. $U_{mn}^{(\mathbf{k})}$ provide a gauge degree of freedom of Wannier functions; it is not determined uniquely and different choice does not affect any physically observable properties. This prevented Wannier functions from being widely used in practical electronic structure calculations.

Marzari and Vanderbilt developed a unique way to determine $U_{mn}^{(\mathbf{k})}$ in their seminal work [MV97] so that the spread function Ω is minimized. The spread

function Ω is the amount of spatial spread of the Wannier function, and is defined by

$$\Omega = \sum_n [\langle w_{n\mathbf{0}} | \mathbf{r}^2 | w_{n\mathbf{0}} \rangle - |\langle w_{n\mathbf{0}} | \mathbf{r} | w_{n\mathbf{0}} \rangle|^2] \quad (2.18)$$

The total spread can be decomposed into a gauge-invariant term Ω_I and a $\tilde{\Omega}$ that is dependent on the choice of $U_{mn}^{(\mathbf{k})}$. $\tilde{\Omega}$ can be further decomposed into terms diagonal and off-diagonal in the Wannier function basis, Ω_D and Ω_{OD}

$$\Omega = \Omega_I + \Omega_D + \Omega_{OD}. \quad (2.19)$$

The explicit expressions for each terms are given in Ref. [MV97].

For the complex bands which overlap with other irrelevant bands, we need to disentangle the bands from the others to obtain the desirable Wannier function [SMV01]. For this, we first set an energy range that all of the bands are taken inside. For the Bloch states, we perform an unitary transform such that

$$|u_{n\mathbf{k}}^{\text{opt}}\rangle = \sum U_{mn}^{\text{dis}(\mathbf{k})} |u_{m\mathbf{k}}\rangle. \quad (2.20)$$

We minimize the gauge independent spread Ω_I in terms of $U_{mn}^{\text{dis}(\mathbf{k})}$ to get the disentangled Wannier functions. After the Wannier functions are established, we can get the overlap and hopping matrix for the Hamiltonian within Wannier function basis.

2.3 Computational details

We studied $\text{Ba}X\text{O}_3/\text{BBL}/\text{Ba}Y\text{O}_3$ whose crystal structure is shown in Fig. 2.1. It is a perovskite oxide heterostructure of BaBiO_3 -bilayer (BBL) oriented in the (111) direction that is sandwiched by lower layer $\text{Ba}X\text{O}_3$ and upper layer $\text{Ba}Y\text{O}_3$. In Fig. 2.1, only X , Bi, and Y atoms are drawn for clarity. In the BBL, Bi atoms form a buckled honeycomb lattice which consists of two triangular sublattices of upper and lower layers. We used 5 bottom layers and 5 top layers for calculations of symmetric configurations ($X = Y$), and 8 bottom layers and 8 top layers for calculations of asymmetric configurations ($X \neq Y$).

The first-principles calculations were performed using the PAW method and PBE exchange-correlation functional as implemented in VASP code [KF96a, KF96b]. The plane-wave energy cutoff was set for 400 eV, and $12 \times 12 \times 1$ mesh was employed for momentum space sampling. The atomic structures were relaxed with the force criteria of 0.005 eV/Å. The Wannier90 code [MYL+08] was used to construct maximally-localized Wannier functions and to calculate Berry curvatures.

The first-principles Berry curvature is calculated with the linear response Kubo-like formula as implemented in Wannier90 code.

$$\begin{aligned}\Omega(\mathbf{k}) &= \sum_n f_n \Omega_n(\mathbf{k}) \\ \Omega_n(\mathbf{k}) &= -2\text{Im} \sum_{m \neq n} \frac{\langle u_{n\mathbf{k}} | v_x | u_{m\mathbf{k}} \rangle \langle u_{m\mathbf{k}} | v_y | u_{n\mathbf{k}} \rangle}{(E_{n\mathbf{k}} - E_{m\mathbf{k}})^2},\end{aligned}\tag{2.21}$$

where f_n is the Fermi distribution function, $v_{x,y}$ is the velocity operator, and $|u_{n\mathbf{k}}\rangle$ is the periodic part of the energy eigenfunction with eigenvalue $E_{n\mathbf{k}}$.

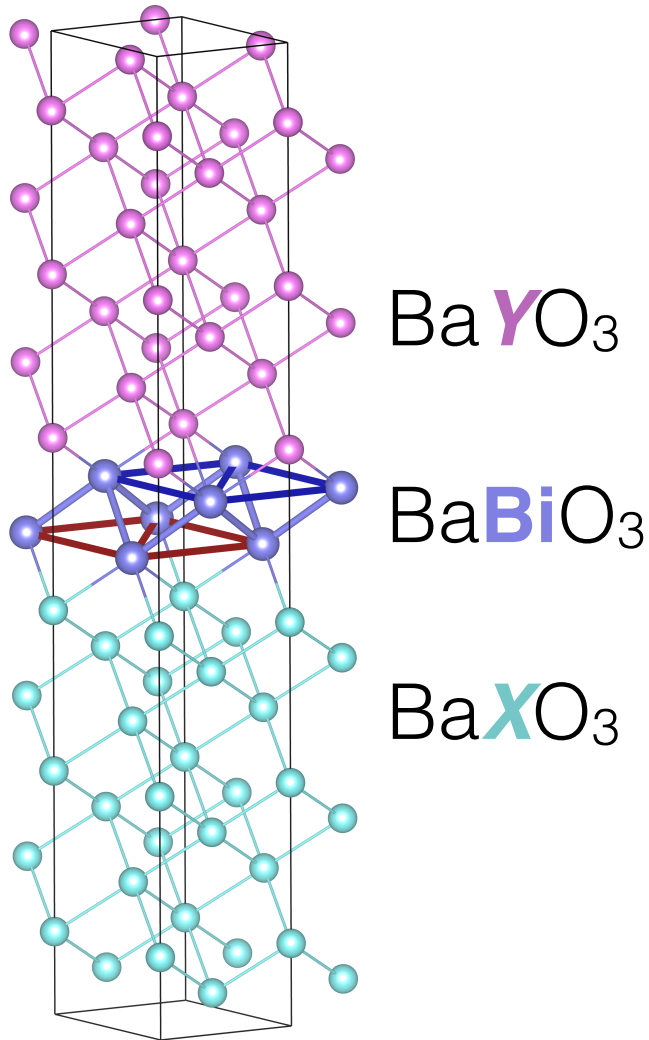


Figure 2.1: The crystal structure of BaXO₃/BBL/BaYO₃. 8 bottom layers of BaXO₃, BaBiO₃-bilayer, and 8 top layers of BaYO₃ are shown. Only X, Bi, and Y atoms are drawn for simplicity. BaBiO₃-bilayer form a buckled honeycomb lattice consists of upper triangular sublattice colored by blue and lower triangular sublattice colored by red.

To verify the topological phase of the system, we first calculated the Wannier functions with the four Bi s projectors (two sublattices and two spin components) that reproduce the band structures near the Fermi level. Then, the tight-binding Hamiltonian of strip geometry is constructed using the obtained Wannier functions and hopping terms. Band structure is calculated with obtained tight-binding Hamiltonian. By counting the number of crossing points in the half Brillouin zone, we verified whether the system is a QSH insulator or not.

Chapter 3

Topological phases in honeycomb system

In this chapter, we give an introduction to the general physics in honeycomb lattice. Tight-binding model describing the single-orbital band in the honeycomb lattice is studied using two representative systems, e.g. graphene and silicene. In particular, silicene, which has a buckled honeycomb lattice, is studied in detail because the buckled structure and SOC allow us to control of degrees of freedom in honeycomb system. Topological phases realized in the honeycomb lattice is illustrated in general terms. Two topological phases, QSH and QVH phases, are given special focus. Here, we mostly follow the notations used in Ref. [Eza15].

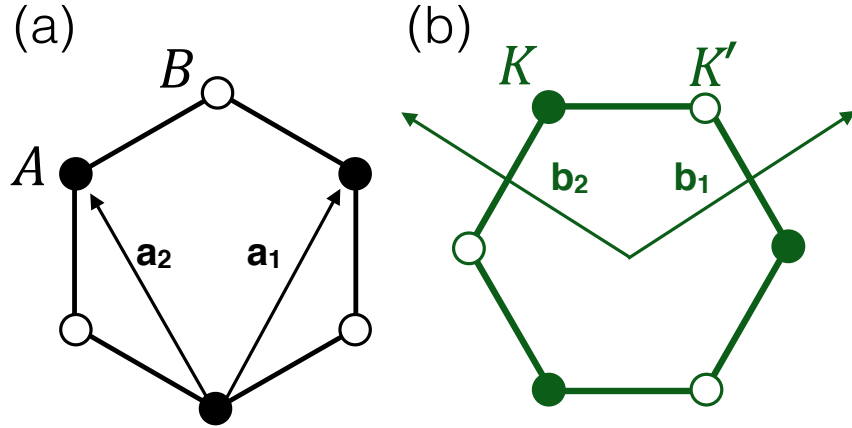


Figure 3.1: (a) Primitive lattice vectors \mathbf{a}_1 and \mathbf{a}_2 for direct lattice. Honeycomb lattice consists of two triangular sublattices denoted by filled-circle A and open-circle B . (b) First Brillouin zone in momentum space with two inequivalent K and K' points. Primitive vectors \mathbf{b}_1 and \mathbf{b}_2 for reciprocal lattice is shown.

3.1 Honeycomb system

The crystal structure of honeycomb systems, e.g. graphene and silicene, is a two dimensional honeycomb lattice that is generated by primitive lattice vectors \mathbf{a}_1 and \mathbf{a}_2 as shown in Fig. 3.1(a). Two triangular lattices denoted by sublattice A and sublattice B constitute the direct lattice (see Fig. 3.1). The reciprocal lattice in the momentum space is also a honeycomb lattice rotated by 30° with respect to the direct lattice, whose first Brillouin zone is shown in Fig. 3.1(b).

3.1.1 Planar structure

The Hamiltonian of planar honeycomb system, which is represented by graphene, is the simplest single-orbital tight-binding model on a honeycomb lattice, which

is given by

$$H = -t \sum_{\langle i,j \rangle s} c_{is}^\dagger c_{js}, \quad (3.1)$$

where c_{is}^\dagger is an creation operator for an electron with spin polarization $s = \uparrow \downarrow$ at site i , $\langle i, j \rangle$ runs over all the nearest neighbor hopping sites, and t is the nearest-neighbor hopping energy.

To obtain the band structure, we need to get the Hamiltonian in the momentum space, in which our main focus is the physics near the Fermi energy. To derive the Hamiltonian, we Fourier transform Eq. 3.1. The results is

$$\begin{aligned} H &= t \sum_s \int d^2k \begin{pmatrix} c_{As}^{k\dagger} & c_{Bs}^{k\dagger} \end{pmatrix} \begin{pmatrix} 0 & f(\mathbf{k}) \\ f^*(\mathbf{k}) & 0 \end{pmatrix} \begin{pmatrix} c_{As}^k \\ c_{Bs}^k \end{pmatrix} \\ &= t \sum_s \int d^2k \begin{pmatrix} c_{As}^{k\dagger} & c_{Bs}^{k\dagger} \end{pmatrix} H(\mathbf{k}) \begin{pmatrix} c_{As}^k \\ c_{Bs}^k \end{pmatrix} \end{aligned} \quad (3.2)$$

with

$$f(\mathbf{k}) = e^{-iak_y/\sqrt{3}} + 2e^{iak_y/2\sqrt{3}} \cos \frac{ak_x}{2}. \quad (3.3)$$

The energy spectrum obtained by diagonalizing the $H(\mathbf{k})$ is

$$E(\mathbf{k}) = t \sqrt{1 + 4 \cos \frac{ak_x}{2} \cos \frac{\sqrt{3}ak_y}{2} + 4 \cos^2 \frac{ak_x}{2}}. \quad (3.4)$$

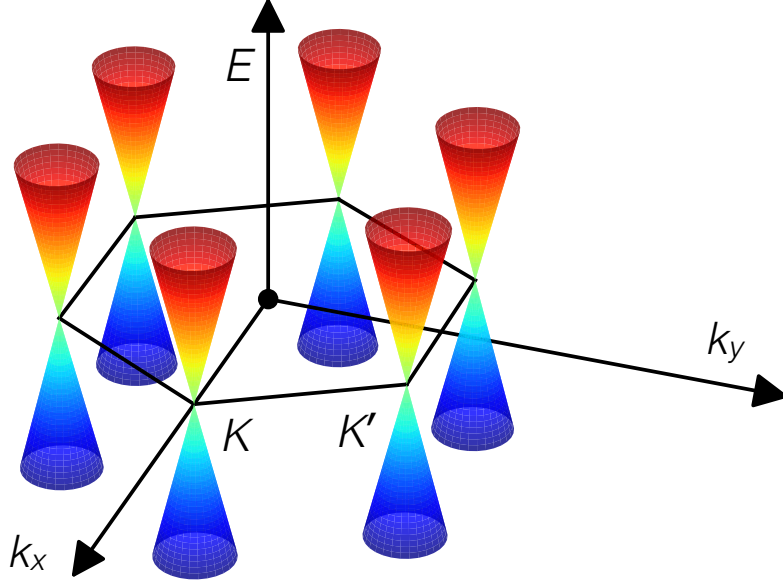


Figure 3.2: Low-energy band structure of tight-binding model. Six Dirac cones are located at the corners of the first Brillouin zone with the Fermi level touching gap closing points.

Note that the gap closes at the K_η point that is defined by

$$K_\eta = \left(\eta \frac{4\pi}{3a}, 0 \right) \quad \text{with } \eta = \pm 1. \quad (3.5)$$

The K_+ and K_- points are identical to the K and K' points, respectively.

The low-energy band structure obtained by diagonalizing the Hamiltonian is illustrate in Fig. 3.2. It consists of 6 Dirac cones near the Fermi energy. The cones touch the Fermi energy at two inequivalent points, that is, the K and K' points in the Brillouin zone (see Fig. 3.1). Because the dispersion relation is linear around these points, they are called the Dirac points.

Near the the K_η point, the Hamiltonian is approximated to the linear order in \mathbf{k} by

$$H^\eta = \sum_s \int d^2k \begin{pmatrix} c_{As}^{\eta\dagger} & c_{Bs}^{\eta\dagger} \end{pmatrix} H_s^\eta \begin{pmatrix} c_{As}^\eta \\ c_{Bs}^\eta \end{pmatrix}, \quad (3.6)$$

with

$$H_s^\eta = \hbar v_F \begin{pmatrix} 0 & \eta k_x - i k_y \\ \eta k_x + i k_y & 0 \end{pmatrix} = \hbar v_F (\eta k_x \tau_x + k_y \tau_y), \quad (3.7)$$

where $\boldsymbol{\tau} = (\tau_x, \tau_y, \tau_z)$ is the Pauli matrix for the sublattice pseudospin A and B , and $v_F = \frac{\sqrt{3}}{2\hbar} a t$ is the Fermi velocity with a being the lattice constant. The dispersion relation is linear for \mathbf{k} . We call the H_s^η as the Dirac Hamiltonian.

3.1.2 Buckled structure

The tight-binding Hamiltonian of silicene, a buckled honeycomb system, is also described by the Eq. 3.1. There are, however, two distinctive features that make the silicene crucially different from graphene. One is its buckled structure as shown in Fig. 3.3 with a layer separation between the two sublattices A and B . This freedom allows us to tune the bandgap by introducing a potential difference between the two sublattices by perpendicular electric field [DZF12, NLT⁺11]. The other is the presence of the spin-orbit coupling, which could turn silicene to a topological insulator [LFY11]. It is noted that larger spin-orbit coupling in silicene compared to that in graphene can be also attributed

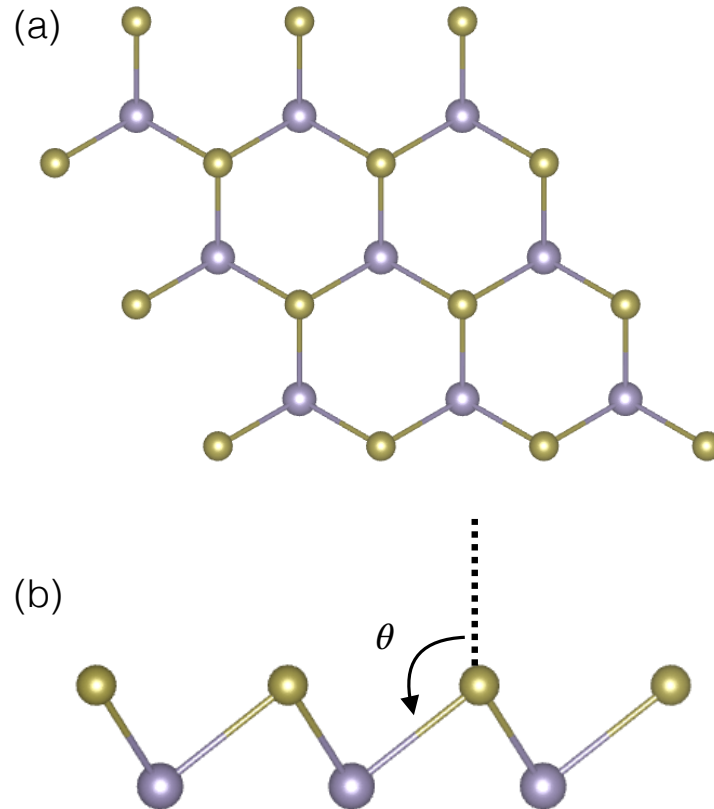


Figure 3.3: (a) Top view and (b) side view of the crystal structure of buckled honeycomb lattice. Two sublattices are distinguished by different colors. The buckling angle θ is defined in (b). The angle is exaggerated in (b) for silicene.

to the silicene's buckled structure [LFY11].

When we apply electric field E_z perpendicular to silicene, the tight-binding Hamiltonian becomes

$$\begin{aligned}
H = & -t \sum_{\langle i,j \rangle_s} c_{is}^\dagger c_{js} + i \frac{\lambda_{SO}}{3\sqrt{3}} \sum_{\langle\langle i,j \rangle\rangle_s} \nu_{ij} c_{is}^\dagger s c_{js} \\
& - \ell \sum_{is} \mu_i E_z c_{is}^\dagger c_{is},
\end{aligned} \tag{3.8}$$

where $\langle\langle i,j \rangle\rangle$ run over all the next-nearest neighbor hopping sites. The spin index stands for $s = \uparrow\downarrow$ for indices and for $s = \pm$ within equations.

Here, we explain each term in Eq. 3.8. (i) The first term is the usual nearest-neighbor hopping with the hopping energy t , which is responsible for massless Dirac cone. (ii) The second term represents the effective spin-orbit coupling with λ_{SO} , where $\nu_{ij} = +1$ if the next-nearest-neighboring hopping is anticlockwise, and $\nu_{ij} = -1$ if it is clockwise with respect to the positive z -axis [KM05]. We note that a large spin-orbit interaction with $\lambda_{SO} = 0.3$ eV could be materialized in functionalized stanene [XYZ⁺13], which will be a topological insulator at room temperature. (iii) The third term represents the staggered sublattice potential with $\mu_i = +1(-1)$ for the A (B) site.

The low-energy physic near the Fermi energy is described by the Dirac theory, which is constructed just as in the case of graphene. We rewrite the Hamiltonian Eq. 3.8 in the form of Eq. 3.6. The Dirac Hamiltonian is explicitly given by

$$H_s^\eta = \begin{pmatrix} \Delta_s^\eta & \hbar v_F (\eta k_x - i k_y) \\ \hbar v_F (\eta k_x + i k_y) & -\Delta_s^\eta \end{pmatrix} \tag{3.9}$$

where

$$\Delta_s^\eta = \eta s \lambda_{SO} - \ell E_z \equiv -\ell (E_z - \eta s E_{cr}) \quad (3.10)$$

with

$$E_{cr} \equiv \lambda_{SO}/\ell \quad (3.11)$$

Hamiltonian can be indexed by η and s . Note that Δ_s^η acts as the Dirac mass. The energy spectrum reads

$$E(\mathbf{k}) = \pm \sqrt{(\hbar v_F k)^2 + (\Delta_s^\eta)^2}, \quad (3.12)$$

where the momentum is measured from K or K' . The gap is given by $2|\Delta_s^\eta| = 2\ell|E_z - \eta s E_{cr}|$.

It is important that the band gap is tunable by controlling external electric field E_z . The gap is open when $E_z = 0$. As $|E_z|$ increases, the gap become narrower, and it closes at $E_z = \eta s E_{cr}$, where silicene become semimetallic just as in graphene. As $|E_z|$ increases further, the gap opens again.

3.1.3 Dirac mass terms

There are actually other ways to control the bandgap by introducing other interactions to silicene. Since each Dirac cone is indexed by two parameters $\eta = \pm$ and $s = \pm$, the most general Dirac mass could have the following expression

$$\Delta_s^\eta = \eta s \lambda_{SO} - \lambda_V + \eta \lambda_H + s \lambda_{SX}, \quad (3.13)$$

so that it has four independent parameters, λ_{SO} , λ_V , λ_H , and λ_{SX} . We have already discussed the first two terms representing the spin-orbit interaction and the sublattice staggered potential with $\lambda_V = lE_z$. We may write down the tight-binding terms that yield the fourth and fifth terms,

$$i \frac{\lambda_H}{3\sqrt{3}} \sum_{\langle\langle i,j \rangle\rangle_s} \mu_{ij} c_{is}^\dagger c_{js}, \quad i\lambda_{SX} \sum_{is} s\mu_i c_{is}^\dagger c_{is} \quad (3.14)$$

The fourth term describes the Haldane interaction induced by the photo-irradiation. The fifth term describes the antiferromagnetic exchange magnetization.

Here we note that there are a variety of 2D materials whose low-energy physics is described by the Dirac Hamiltonian Eq. 3.9 with the Dirac mass Eq. 3.13. We call them general honeycomb systems. Examples are monolayer antiferromagnetic manganese chalcogenophosphates (MnPX_3 , $X = \text{S, Se}$) and perovskite G-type antiferromagnetic insulators grown along [111] direction [LWH13]. The BBL heterostructure investigated in this thesis is also fall into this category.

In what follows we analyze the Dirac Hamiltonian Eq. 3.9 with the Dirac mass Eq. 3.13. It can be positive, negative or zero. The band gap is given by $2|\Delta_s^\eta|$.

3.2 Topological phases

3.2.1 Chern numbers

For any insulating state $|\psi(\mathbf{k})\rangle$ we may define a gauge potential in the momentum space by

$$a_k(\mathbf{k}) = -i\langle\psi(\mathbf{k})|\partial_k|\psi(\mathbf{k})\rangle \quad (3.15)$$

which is called the Berry connection. Then we may define the gauge-invariant “magnetic field” in the momentum space, which is properly called the Berry curvature $F(\mathbf{k})$,

$$F(\mathbf{k}) = \frac{\partial}{\partial k_x} a_y(\mathbf{k}) - \frac{\partial}{\partial k_y} a_x(\mathbf{k}). \quad (3.16)$$

The Chern number is the integral of the Berry curvature $F(\mathbf{k})$ over the first Brillouin zone, which is the total “magnetic flux”,

$$\mathcal{C} = \frac{1}{2\pi} \int d^2k F(\mathbf{k}). \quad (3.17)$$

The Berry curvature is strictly localized at the K and K' points. This feature remains unchanged even if we include the extra terms Eq. 3.14. Consequently, the Dirac Hamiltonian is valid to make a topological analysis to each valley. The Chern number is indexed by the spin $s = \uparrow\downarrow$ and the valley index $\eta = \pm$. Namely, it is possible to assign the Chern number \mathcal{C}_s^η to each valley.

When the Hamiltonian is given by Eq. 3.9, the Berry curvature can be

explicitly calculated for each valley as

$$F_s^\eta(\mathbf{k}) = -\eta \frac{\Delta_s^\eta}{2 \left((\hbar v_F k)^2 + (\Delta_s^\eta)^2 \right)^{3/2}}. \quad (3.18)$$

The Chern number, which is the integration of the Berry curvature, is obtained as

$$C_s^\eta = -\frac{\eta}{2} \text{sgn}(\Delta_s^\eta) \quad (3.19)$$

where the Dirac mass Δ_s^η can be of a general form. It is important to note that only the sign of the mass term is important in determining the Chern number.

The Chern number is quantized as $C_s^\eta = \pm \frac{1}{2}$. It is insensitive to a deformation of the band structure provided that the gap is open. On the other hand, it changes its sign as the Dirac mass Δ_s^η changes its sign. Such a quantity is a topological charge. Hence an insulator phase is indexed by a set of four Chern numbers C_s^η . A topological phase transition occurs when the sign of the Dirac mass Δ_s^η changes.

It is instructive to make a re-interpretation of the Chern number [HK10, QZ11]. When the Hamiltonian is given in terms of the 2×2 Hamiltonian as in Eq. 3.9, or $H_s^\eta = \boldsymbol{\tau} \cdot \mathbf{d}$ with $d_x = \eta \hbar v_F k_x$, $d_y = \hbar v_F k_y$, $d_z = \Delta_s^\eta$, the Chern number C_s^η is equivalent to the Pontryagin number,

$$C_s^\eta = \frac{1}{4\pi} \int d^2k \left(\frac{\partial \hat{\mathbf{d}}}{\partial k_x} \times \frac{\partial \hat{\mathbf{d}}}{\partial k_y} \right) \cdot \hat{\mathbf{d}} \quad (3.20)$$

The Pontryagin number is a topological number which counts how many times

the vector $\hat{\mathbf{d}}$ wraps a sphere. Using the polar coordinate of the $\hat{\mathbf{d}}$ vector, $\hat{d}_x \pm i\hat{d}_y = \sqrt{1 - \sigma^2(\mathbf{k})}e^{i\eta\theta}$, $\hat{d}_z = \sigma(\mathbf{k})$, we obtain

$$\mathcal{C}_s^\eta = \frac{\eta}{4\pi} \int d^2k \epsilon_{ij} \partial_i \sigma \partial_j \theta = -\frac{\eta}{2} \int_0^1 d\sigma \quad (3.21)$$

which agrees with Eq. 3.19. The pseudospin texture forms a meron structure in the momentum space. A meron is a topological structure which has a half integer Pontryagin number.

3.2.2 Classification of topological insulators

We have defined four Chern numbers \mathcal{C}_s^η . Equivalently we may define the total Chern number \mathcal{C} , the spin Chern number \mathcal{C}_s [Pro09, SWSH06, YXS⁺11], the valley Chern number \mathcal{C}_v [ZJF⁺11, ZMM13, LMBM10], and the spin-valley Chern number \mathcal{C}_{sv} [ZJF⁺11]

$$\mathcal{C} = \mathcal{C}_\uparrow^K + \mathcal{C}_\uparrow^{K'} + \mathcal{C}_\downarrow^K + \mathcal{C}_\downarrow^{K'} \quad (3.22)$$

$$\mathcal{C}_s = \frac{1}{2} \left(\mathcal{C}_\uparrow^K + \mathcal{C}_\uparrow^{K'} - \mathcal{C}_\downarrow^K - \mathcal{C}_\downarrow^{K'} \right) \quad (3.23)$$

$$\mathcal{C}_v = \mathcal{C}_\uparrow^K - \mathcal{C}_\uparrow^{K'} + \mathcal{C}_\downarrow^K - \mathcal{C}_\downarrow^{K'} \quad (3.24)$$

$$\mathcal{C}_{sv} = \frac{1}{2} \left(\mathcal{C}_\uparrow^K - \mathcal{C}_\uparrow^{K'} - \mathcal{C}_\downarrow^K + \mathcal{C}_\downarrow^{K'} \right) \quad (3.25)$$

Here we comment that the valley Chern number and the spin-valley Chern number are well defined only in the Dirac theory. Namely, they are ill defined in general tight-binding model. Hence, we may call \mathcal{C} and \mathcal{C}_s the genuine Chern numbers.

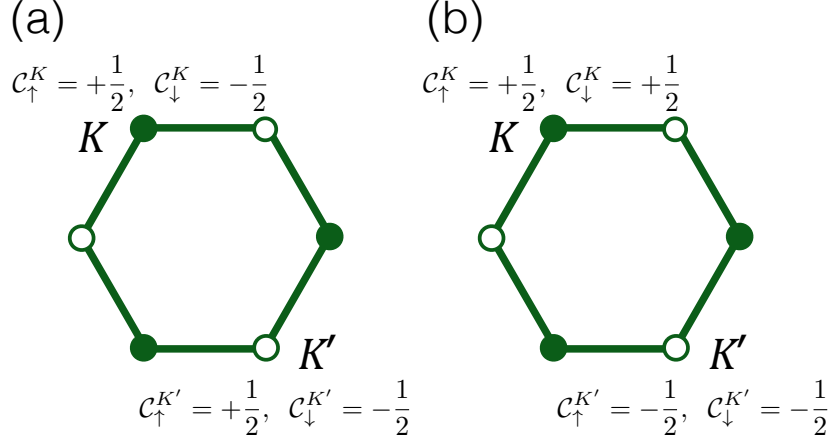


Figure 3.4: Chern numbers distributions for (a) QSH and (b) QVH phases.

Possible sets of genuine Chern numbers $(\mathcal{C}, \mathcal{C}_s)$ are $(0, 0)$, $(2, 0)$, $(0, 1)$, $(1, 1)$ up to the sign \pm . They are the trivial, quantum anomalous Hall, quantum spin Hall, spin-polarized quantum anomalous Hall insulators, respectively. Note that there are two-types of trivial band insulators, which are quantum valley Hall insulator [TQY⁺11, QJL⁺12], and quantum spin-valley Hall (QSVH) insulator with antiferromagnetic (AF) order [Eza13].

The Chern numbers of quantum spin Hall phase and quantum valley Hall phases are shown in Fig. 3.4. These topological phases are shown to be realized in the BBL heterostructure. In the next chapter we discuss in detail how the Dirac mass is controlled in BBL heterostructure to produce these topological phases.

We comment on the relation between the spin Chern number and the \mathbb{Z}_2

index given by [FK06]

$$\mathbb{Z}_2 = \frac{1}{2\pi} \left[\int_{\partial\text{HBZ}} d\mathbf{k} \cdot \mathbf{A}(\mathbf{k}) - \int_{\text{HBZ}} d^2k F(\mathbf{k}) \right] \text{mod}(2). \quad (3.26)$$

The spin Chern number \mathcal{C}_s is identical to the \mathbb{Z}_2 index by modulo 2 when there exists the time-reversal symmetry [Pro09]. The spin Chern number is well defined even when there is no time-reversal symmetry, while the \mathbb{Z}_2 index is well defined even when s_z is not a good quantum number.

Chapter 4

Electronic structures of BBL heterostructures

This chapter deals with first-principles calculation results of BBL heterostructure. The perovskite heterostructure of BBL grown along the (111) direction is shown to host QSH and QVH phases with appropriate choices of neighboring layers. In addition, we suggest a ferroelectric control of topological phases in $\text{BaTiO}_3/\text{BBL}/\text{BaTiO}_3$ heterostructure where the QSH and QVH phases can be selected via switching the polarization directions of BaTiO_3 layer.

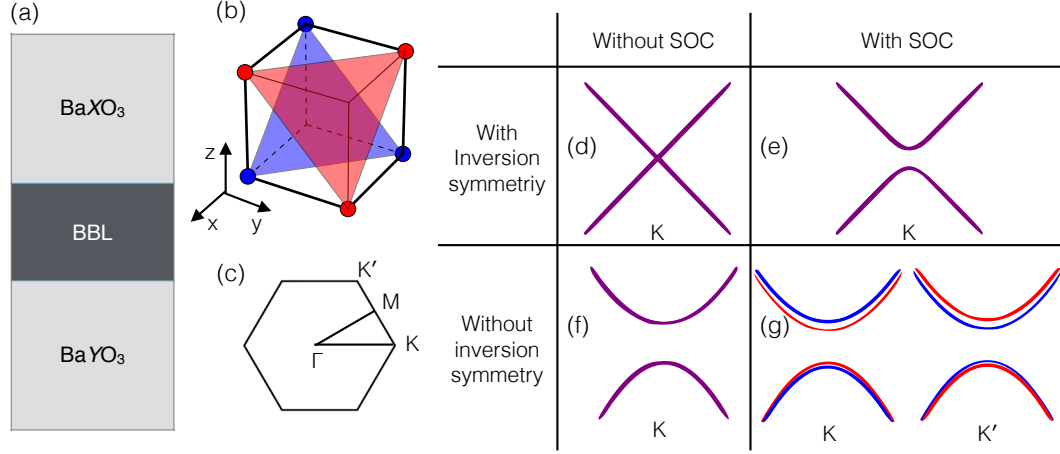


Figure 4.1: (a) The schematic picture of $\text{BaXO}_3/\text{BaBiO}_3/\text{BaYO}_3$ along the (111) direction investigated in this study. (b) The (111)-oriented BBL form a buckled honeycomb lattice consisting of red and blue triangular sublattices. (c) 2D hexagonal Brillouin zone and high symmetry points. (d)-(g) Schematic band structures emerging from the (111)-oriented BBL heterostructures in terms of SOC and inversion symmetry.

4.1 (111)-oriented BaBiO_3 heterostructure

As an ideal platform for Dirac Fermions and engineering of its various degrees of freedom, we consider a perovskite oxide heterostructure of BaBiO_3 -bilayer (BBL) oriented in the (111) direction that is sandwiched by lower layer BaXO_3 and upper layer BaYO_3 . We denote this structure $\text{BaXO}_3/\text{BBL}/\text{BaYO}_3$ whose structure is shown schematically in Fig. 4.1(a). In the (111)-oriented BBL, Bi atoms form a buckled honeycomb lattice which consists of two triangular sublattices of upper and lower layers as illustrated in Fig. 4.1(b).

Two wide bandgap semiconductors BaXO_3 and BaYO_3 sandwich the BBL. As the charge state of Bi in perovskite BaBiO_3 structure is Bi^{4+} (see Fig. 4.2),

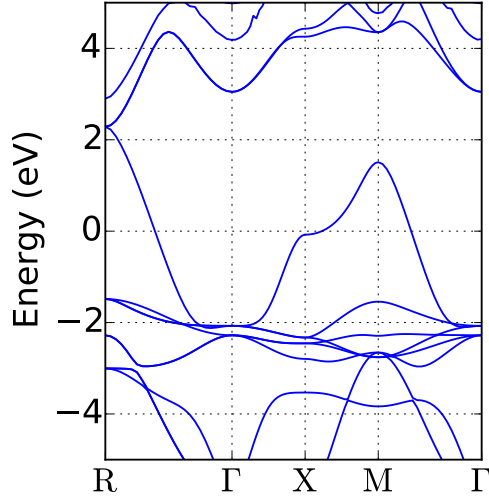


Figure 4.2: Band structure of perovskite BaBiO₃. Bi-6s band has a large bandwidth and cross the Fermi level.

we expect, when incorporated in the heterostructure, the half-filled Bi 6s band, originating from the BBL, is positioned within bandgaps of the sandwich layers. In addition, the choices of sandwich layers are directly linked to the inversion symmetry of BBL. When the X and Y are the same atoms (symmetric configuration), the inversion symmetry of the BBL is conserved, while the different top and bottom layers (asymmetric configuration) brings the structural inversion asymmetry (SIA) and break the inversion symmetry of the BBL. In the present paper, we mainly focus on the inversion symmetry of the BBL heterostructures. The overview of the obtained band structure is drawn in Fig. 4.1(d)-(g). In the following sections, we study these band structure in detail. The time-reversal symmetry (TRS) remains intact as we investigate only the non-magnetic layers.

4.2 Emergence of a s -orbital Dirac cone

We first examine the symmetric configuration where the BBL is embedded in the same top and bottom layers. In this configuration, Bi atoms in two sublattices are in the same environments, and consequently, the inversion symmetry of the BBL is preserved. We find that a Dirac cone is emerging from the BBL in the symmetric configuration. The low-energy band structure is dominantly composed of Bi-6s orbitals and is well described by the tight-binding model for single s -orbital band at the 2D hexagonal lattice. The Dirac Hamiltonian near the K and K' points is described by

$$H^n = \hbar v_F (\eta k_x \tau_x + k_y \tau_y) \otimes \sigma_0, \quad (4.1)$$

where $\eta = \pm 1$ for valleys K , K' , and τ_i , σ_i are the Pauli matrices for the real spin and the sublattice pseudospin, respectively. τ_0 and σ_0 are unit matrices acting on corresponding subspaces. The 2D s -orbital Dirac cone emerging in the BBL is a perfect replication of the graphene band structure apart from the fact that Bi-6s orbitals plays the same role in BBL as carbon- $2p_z$ orbitals does in graphene. Further, the BBL heterostructure suggested in the present study allows us to introduce various mass terms to the Hamiltonian of Eq. 4.1, which will be discussed throughout the thesis.

We show the band structure of BaZrO₃/BBL/BaZrO₃ without spin-orbit coupling in Fig. 4.3(a). Even though the Bi-6s band has a large bandwidth in its bulk structure (see Fig. 4.2), the s -orbital Dirac cone originating from the BBL is confined within the buckled honeycomb lattice and almost decoupled from the neighboring layers, which suggests a 2D nature of the Dirac Fermion.

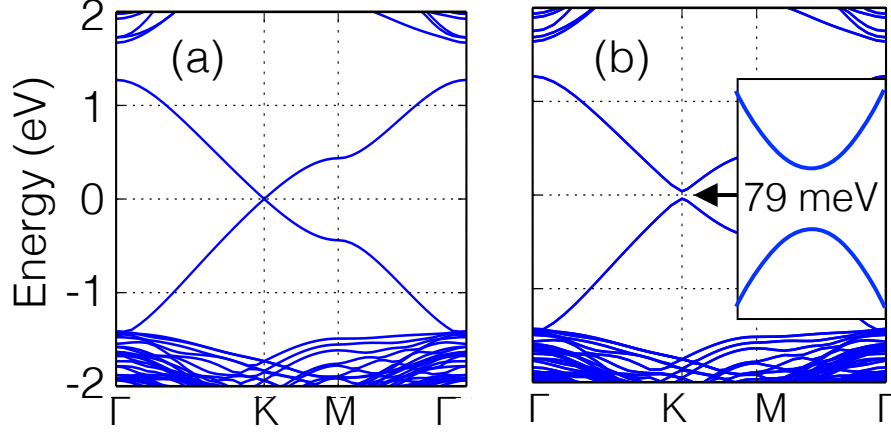


Figure 4.3: Band structure of BaZrO₃/BBL/BaZrO₃ (a) with and (b) without the SOC. (a) Band structure shows a massless Dirac cone near the K point. The Dirac cone is decoupled from the sandwich layers bands. (b) SOC opens the gap at the K point by 79 meV.

Furthermore, the Fermi level is touching the Dirac point without need to introduce additional electrons or holes to the system.

4.3 Symmetric configuration:

Quantum spin Hall insulator

When the SOC is included, the Dirac cone acquires a mass and opens a gap. Opening of a bandgap by SOC in otherwise a semi-metallic Dirac cone is the indication of the Kane-Mele type topological insulator. The non-trivial mass term, $\lambda_{SO}\eta\tau_z \otimes \sigma_z$, which turns the system to the QSH insulator is added in

Eq. 4.1, where $2\lambda_{SO}$ is the non-trivial bandgap at the K point.

$$H^n = \hbar v_F(\eta k_x \tau_x + k_y \tau_y) \otimes \sigma_0 + \lambda_{SO} \eta \tau_z \otimes \sigma_z \quad (4.2)$$

At this point, to understand the behavior of various mass terms with respect to the symmetry operations, we discuss the effect of inversion operation ($\mathcal{P} : \mathbf{k} \rightarrow -\mathbf{k}$) and time-reversal operation ($\mathcal{T} : \mathbf{k} \rightarrow -\mathbf{k}, \mathbf{s} \rightarrow -\mathbf{s}$) on Pauli matrices for pseudo-spin τ_i , real spin σ_i , and valley index η . Firstly, inversion operation takes sublattice A into B and vice versa, so that we have

$$\mathcal{P} : \tau_z \rightarrow -\tau_z. \quad (4.3)$$

And it is noted that under \mathcal{P} , $\tau_x \rightarrow \tau_x$ and $\tau_y \rightarrow -\tau_y$. Also \mathcal{P} takes K to K' ,

$$\mathcal{P} : \eta \rightarrow -\eta. \quad (4.4)$$

But real spins are not affected by \mathcal{P} ,

$$\mathcal{P} : \sigma_i \rightarrow \sigma_i. \quad (4.5)$$

Next, we observe that the \mathcal{T} change the sign of momenta, but does not affect the sublattice degree of freedom,

$$\mathcal{T} : \eta \rightarrow -\eta, \tau_i \rightarrow \tau_i. \quad (4.6)$$

And σ_z , the z -component of the spin Pauli matrix, transforms according to

$$\mathcal{T} : \sigma_z \rightarrow -\sigma_z. \quad (4.7)$$

Therefore the mass term $\lambda_{SO}\eta\tau_z \otimes \sigma_z$, which is a simplified version of spin-orbit interaction in the system, is invariant under \mathcal{T} , \mathcal{P} . The mass term should conserve symmetry of the physical system.

The band structure of BaZrO₃/BBL/BaZrO₃ with the inclusion of SOC is shown in Fig. 4.3(b) that exhibit 79 meV of bandgap. It is noted that s_z is not a good quantum number in BBL heterostructures, where the additional spin-mixing terms exist in addition to the Eq. 4.2 (see Chapter 5), but this term is small near the K points and does not modified the topological states because the band gap remains open even with the inclusion of the spin-mixing terms.

To verify the topological state of the system, we first calculated the Wannier functions with the four Bi s projectors (two sublattices and two spin components) that reproduce the band structures near the Fermi level. Then the tight-binding Hamiltonian of strip geometry is constructed using the obtained Wannier functions and hopping terms, and its band structure is calculated. The QSH phase of the system is confirmed by the strip geometry calculation whose band structure is shown in Fig. 4.4(a) for zigzag edge and Fig. 4.4(b) for armchair edge, respectively. They exhibit odd number of crossing in the half Brillouin zone as expected from QSH phase.

We calculated electronic structures of various symmetric configurations and tabulated their lattice parameters and bandgaps in Table 4.1. For all the listed

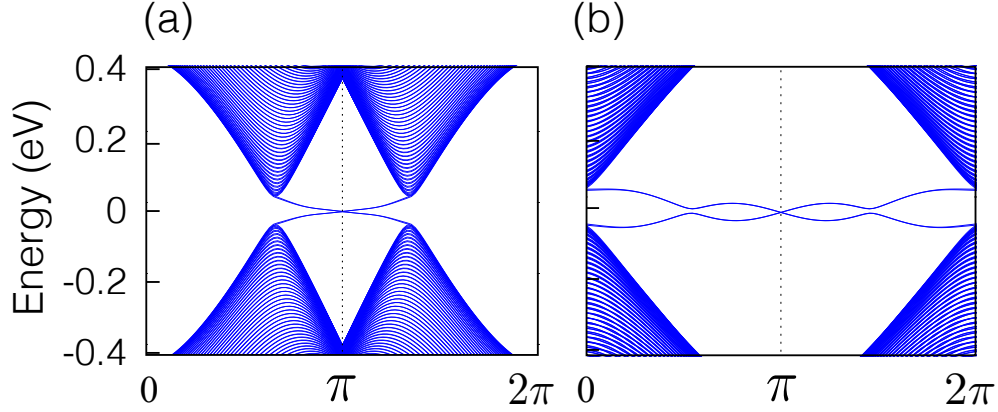


Figure 4.4: Topologically protected edge states of $\text{BaZrO}_3/\text{BBL}/\text{BaZrO}_3$ for (a) zigzag edge and (b) armchair edge. The strip geometry is constructed with hopping parameters obtained from Wannier function method. Both edges states cross the Fermi level odd times in the half Brillouin zone.

structures 5 lower layers and 5 upper layers were included and cell parameters as well as the internal coordinates were relaxed. We find that the all the heterostructures listed in Table 4.1 are QSH insulators with relatively large non-trivial bandgaps. Remarkably, contrary to the common notion that the SOC effect is negligible in s -orbital system, quite large SOC gap is obtained. We will explain the origin of the large SOC gap in the Chapter 6 after we construct tight-binding Hamiltonian in Chapter 5. As these bandgaps are much larger than the room temperature, if the heterostructure is fabricated with good crystal quality, the QSH phase could be detected in experiments. This, to our best knowledge, is the first Kane-Mele type topological insulator [KM05] realized in s -orbital systems.

We also carried out similar calculation for Sr-based system, where all Ba atoms are replaced by Sr atoms. The results are summarized in Table 4.2. We

Table 4.1: Lattice parameters and SOC gap at K for Ba-based system.

Sandwich layer	Lattice constant (\AA)	Bucking angle ($^\circ$)	SOC gap at K (meV)
BaTiO ₃	5.78	129.45	91
BaZrO ₃	6.05	127.19	79
BaSnO ₃	5.97	127.55	72
BaHfO ₃	5.98	127.79	49
BaCeO ₃	6.31	125.14	60

Table 4.2: Lattice parameters and SOC gap at K for Sr-based system.

Sandwich layer	Lattice constant (\AA)	Bucking angle ($^\circ$)	SOC gap at K (meV)
SrTiO ₃	5.64	130.24	102
SrZrO ₃	5.96	127.19	98
SrSnO ₃	5.87	127.79	81
SrHfO ₃	5.87	128.26	59
SrCeO ₃	6.23	127.58	45

observe that Sr-based system have smaller lattice constants and larger SOC gap (except for the Ce case). This give us a hint that the lattice parameter is a important factor in determining the SOC gap. The detailed explanation the SOC gap will be given after we construct tight-binding Hamiltonian in Chapter 5.

It is noted that the heterostructures with BaSnO₃ and SrSnO₃ layers show metallic band structure in PBE calculations, but have gaps at K point. This is because the systems containing Sn atoms are notorious for their unexpectedly large bandgap underestimation. As a results, the bandgap of sandwich layers become very small that make the system a metal. But if we employ hybrid functional or other higher-level calculation methods, it is expected that the systems will become a topological insulator.

4.4 Asymmetric configuration: Quantum valley Hall insulator

The hexagonal system has a valley degree of freedom K and K' . For the symmetric configurations investigated for far, the band structures at the K and K' are identical due to the inversion symmetry as well as the TRS. With different top and bottom layers, however, the SIA break the inversion symmetry of the BBL. It results in a energy difference between sublattices and adds a mass term of $\frac{\Delta}{2}\tau_z \otimes \sigma_0$ to the Hamiltonian Eq. 4.1, where Δ is the trivial bandgap induced by the inversion symmetry breaking.

$$H^n = \hbar v_F(\eta k_x \tau_x + k_y \tau_y) \otimes \sigma_0 + \frac{\Delta}{2} \tau_z \otimes \sigma_0 \quad (4.8)$$

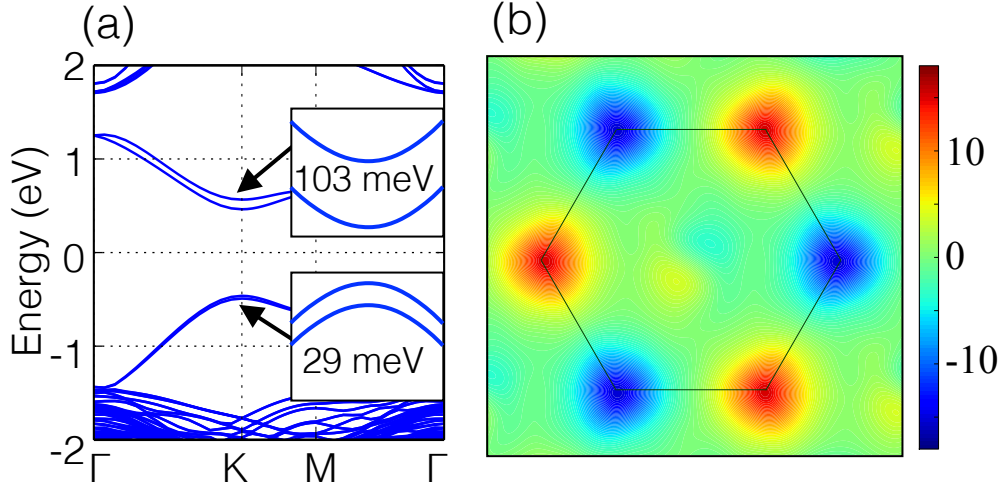


Figure 4.5: (a) Band structure of $\text{BaHfO}_3/\text{BBL}/\text{BaZrO}_3$. Trivial bandgap is 0.924 eV. Valence band is split by 29 meV and Conduction band is split by 103 meV due to the SOC. (b) Calculated Berry curvature are drawn with color code. Atomic units are used. Berry curvature at K and K' are exactly opposite, which confirms the QVH phase.

It leads to QVH phase characterized by valley-contrasting Berry curvatures as shown in Fig. 4.5(b) for $\text{BaHfO}_3/\text{BBL}/\text{BaZrO}_3$. In addition to the trivial bandgap, the band structure exhibit spin-split conduction and valence bands owing to the large SOC of Bi atom. The Berry curvatures and spin-splittings at the K and K' are exactly opposite as they are related by TRS. So that the spin-texture is locked to the valley index.

Figure 4.5(a) shows the band structures of $\text{BaHfO}_3/\text{BBL}/\text{BaZrO}_3$ with SOC that exhibit valley-contrasting Berry curvature shown in Fig. 4.5(b), which is the signature of the QVH phase. The band structure shows 0.924 eV of a trivial bandgap, and further the SOC split the valence band by 29 meV and conduction band by 103 meV at the K point. It is noted that the

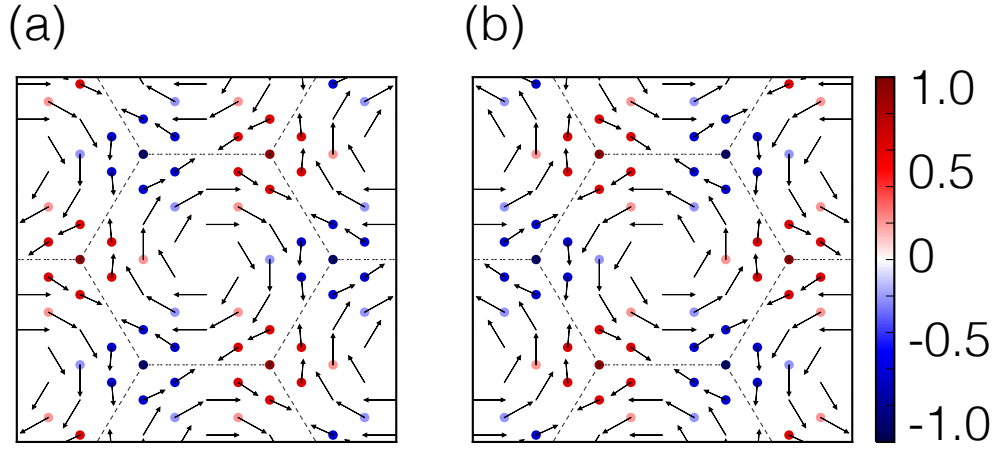


Figure 4.6: In- and out-of-plane spin-texture of $\text{BaHfO}_3/\text{BBL}/\text{BaZrO}_3$ for (a) VBM-1 and (b) VBM. The in-plane spin-texture is represented by arrow and out-of-plane spin-texture is color coded. Chirality of in-plane spin-texture is the same for K and K' while the out-of-plane spin-texture is opposite. The overall spin-texture of VBM is exactly opposite to the that of VBM-1.

larger spin splitting in the conduction than in the valence band is the general characteristic observed in asymmetric configuration of BBL heterostructure.

In addition, the intrinsic Rashba SOC (see Chapter 5) originating from buckled honeycomb structure results in a in- and out-of-plane spin texture [DSSB⁺15, YBS⁺15] as shown in Figs. 4.6(a) and (b) for a band below the valence band maximum (VBM-1) and the valence band maximum (VBM), respectively. The detailed description of the intrinsic Rashba SOC will be discussed in Chapter 5. The in-plane Rashba-like spin textures around K and K' display the same chirality while the out of plane spin polarizations are opposite at K and K' . Also, the VBM-1 and VBM posses exactly opposite spin-textures. (cf. The spin-polarization of the symmetric configuration is hidden due to the inver-

sion symmetry. They are called R-2 and D-2 spin polarizations following the Ref. [ZLL⁺14]). When the top and bottom layers are mutually switched, a complete reversal of the spin-texture is realized, which enables us to control the spin texture in the asymmetric configuration.

We consider the interband matrix elements of the left- and right-circularly polarized light fields (\pm) for a vertical transition from valence band u_v to conduction band u_c [XLF⁺12].

$$\mathcal{P}_{\pm}^{\eta}(k) = \mathcal{P}_x^{\eta}(k) \pm i\mathcal{P}_y^{\eta}(k), \quad (4.9)$$

where $\mathcal{P}_{\alpha}^{\eta}(k)$ ($\alpha = x, y$) is

$$\mathcal{P}_{\alpha}^{\eta}(k) = m_0 \langle u_c(k) | \frac{1}{\hbar} \frac{\partial H}{\partial k_{\alpha}} | u_v(k) \rangle. \quad (4.10)$$

We can obtain an analytic formula near K and K' points,

$$|\mathcal{P}_{\pm}^{\eta}(k)|^2 = m_0^2 v_F^2 \left(1 \pm \eta \frac{\Delta_s^{\eta}}{\sqrt{(\Delta_s^{\eta})^2 + 4a^2 t^2 k^2}} \right)^2. \quad (4.11)$$

We find that K couples to right-circularly polarized light while K' couples to left-circularly polarized light. The valley-dependent spin-splitting, Berry curvatures, and optical selection rule realized in the asymmetric configuration could yield novel transport properties, e.g. valley Hall effect [XYN07], valley spin Hall effect and valley orbital moment Hall effect [XLF⁺12].

4.5 Ferroelectric control of the topological phases

Until now, the control of inversion symmetry of BBL, and resulting QSH and QVH phases are demonstrated in terms of SIA of the heterostructures, i.e. the choice of X and Y elements in sandwich layers. Besides, there is another appealing way to control the inversion symmetry of the BBL even with the same sandwich layers. That is to utilize the bulk inversion asymmetry (BIA) present in ferroelectric materials. The control of polarization directions in sandwich ferroelectric materials can manipulate the inversion symmetry of the BBL considering that the different polarization directions in top and bottom layers effectively provide different environments to Bi atoms in upper and lower sublattices. As a plausible example, let us consider the ferroelectric material BaTiO_3 , which is known to undergoes a structural transform to rhombohedral phase and possesses a $[111]$ polarization in low temperature [KLB93]. In $\text{BaTiO}_3/\text{BBL}/\text{BaTiO}_3$, BaTiO_3 is stabilized with the polarization in $[111]$ direction.

When the polarization direction of top and bottom layers are opposite, the inversion symmetry of the BBL is conserved (see Fig. 4.7(a)) and the QSH phase is induced. The corresponding DFT band structure is shown in Fig. 4.7(c) which shows a Dirac cone with 108 meV non-trivial bandgap. When the top and bottom layers have the same polarization direction as in Fig. 4.7(c), the QVH phase appears. Figure 4.7(d) shows the band structure with 1.17 eV band gap and 192 meV and 56 meV spin splitting for conduction and valence band, respectively. The QVH phase show similar valley-dependent spin-texture and Berry curvature that we observed in Fig. 4.5. And these are completely

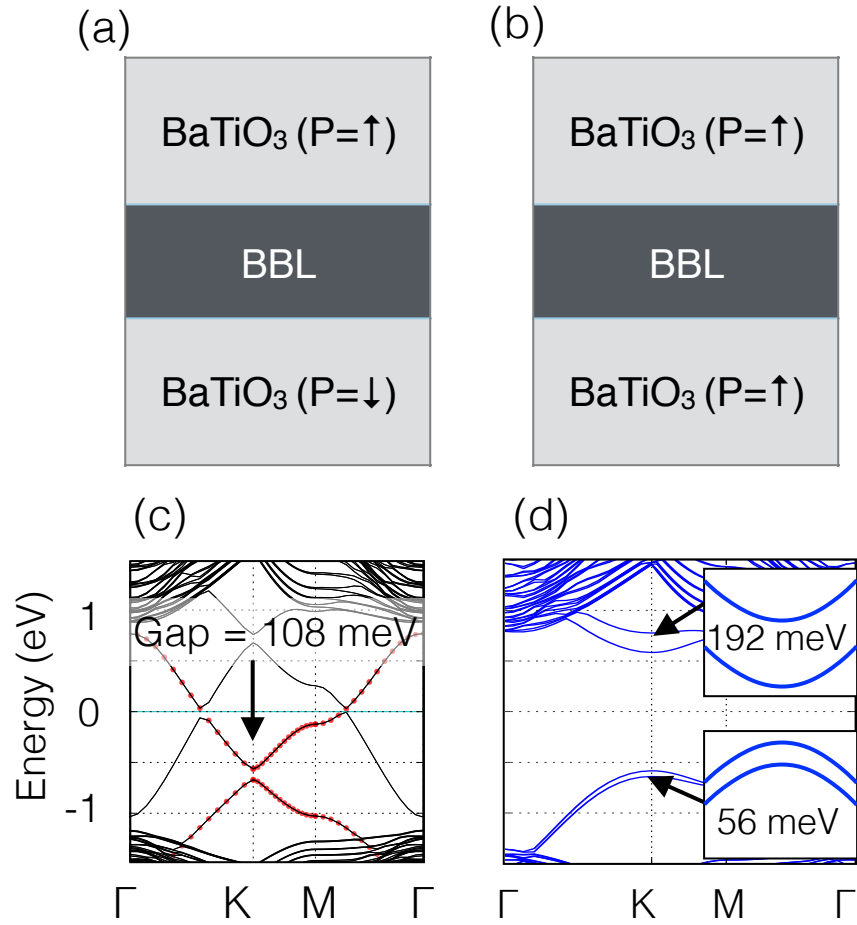


Figure 4.7: (a) The symmetric configuration of BaTiO₃/BBL/BaTiO₃. (b) The asymmetric configuration of BaTiO₃/BBL/BaTiO₃. (c) Band structure of symmetric configuration of BaTiO₃/BBL/BaTiO₃. SOC opens the bandgap by 108 meV. See the text for detailed procedure to obtain this band structure. (d) Band structure of asymmetric configuration BaTiO₃/BBL/BaTiO₃. Trivial bandgap is 1.17 eV. Conduction band and valence band is split by 192 meV and 56 meV, respectively

reversed when the overall polarization direction is reversed.

We describe in detail how the band structure Fig. 4.7(c) is obtained. Due to the periodic supercell approach used in first-principles calculation, ferroelectric configuration Fig. 4.7(a) is problematic. Unphysical electrostatic energy arise at the boundary, so that it is not possible to obtain the symmetric ferroelectric configuration. To overcome this problem we used a double cell geometry as shown in Fig. 4.8(c), in which two ferroelectric configurations are stacked vertically. Using this configuration, we can avoid the unphysical electrostatic energy at the boundary. The whole band structure is projected on upper BBL and lower BBL as shown in Fig. 4.8(a) and (b), respectively. The potential energy is calculated as in Fig. 4.8(d), where the potential gradient due to the polarization is clearly observed.

Topological phases realized in $\text{BaTiO}_3/\text{BBL}/\text{BaTiO}_3$ are controllable if we could switch the polarization direction of one of the two layers. Therefore, it could serve as a unified platform for both QSH and QVH phases. Additionally, topological phases obtained in the heterostructure is non-volatile as long as the polarization is present, which differ from the usual control of topological phases using external electric field.

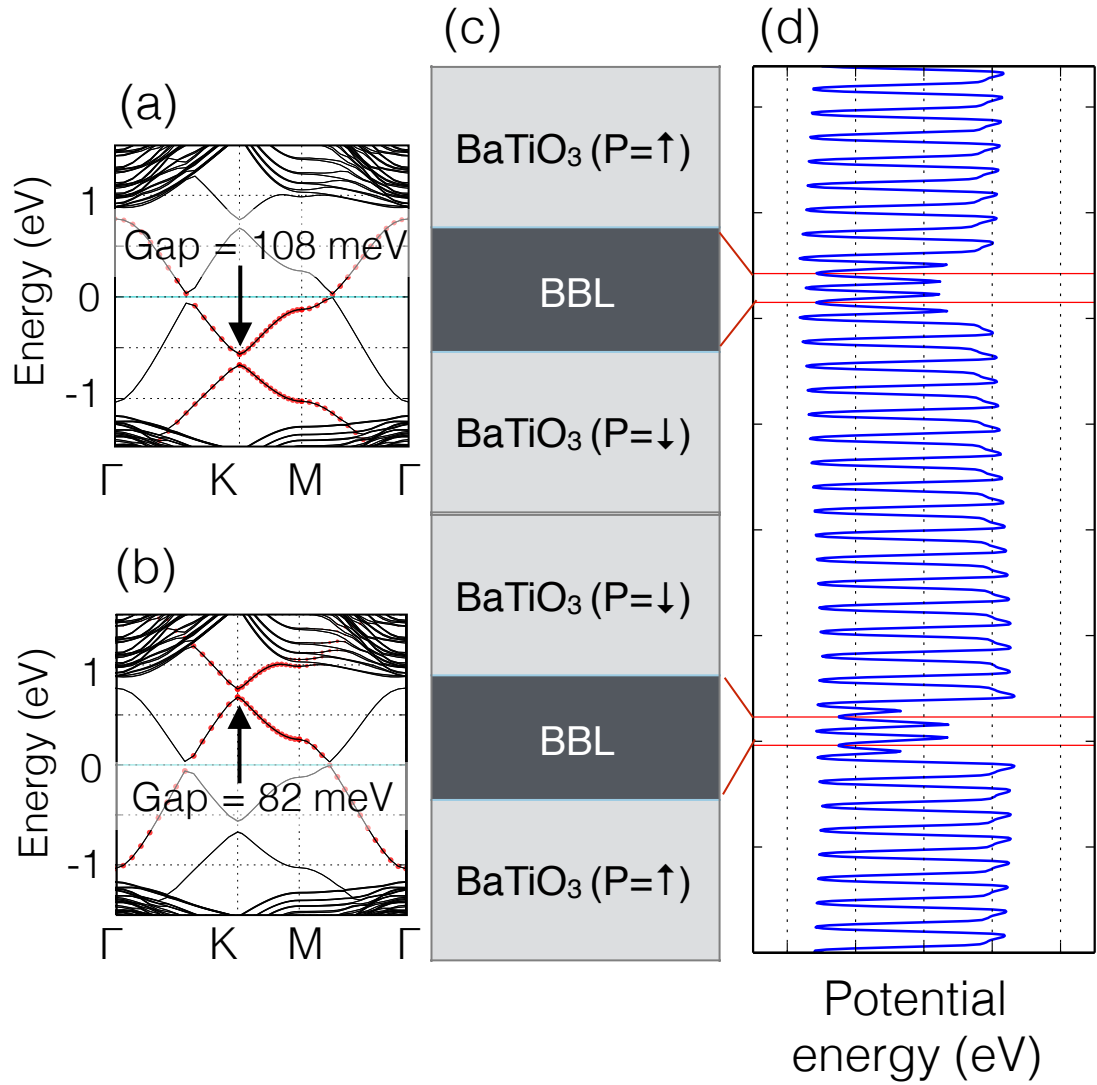


Figure 4.8: Double cell geometry as shown in (c) is used to calculate the band structure of symmetric configuration of BaTiO₃/BBL/BaTiO₃. The total band structure is projected on (a) upper BBL and (b) lower BBL. The projected bands are represented by red color. They correspond to band structures of two symmetric configurations shown in upper part and lower part of (c). (d) Electron potential energy along the (111) direction. Effect of polarization can be seen in potential gradient.

Chapter 5

Tight-binding theory of (111)-oriented BaBiO₃-bilayer heterostructure

This chapter provides Slater-Koster type tight-binding theory of BBL heterostructure. The low energy effective Hamiltonian for *s*-band is obtained from the full tight-binding Hamiltonian. We explain how the large effective SOC is arising in *s* band.

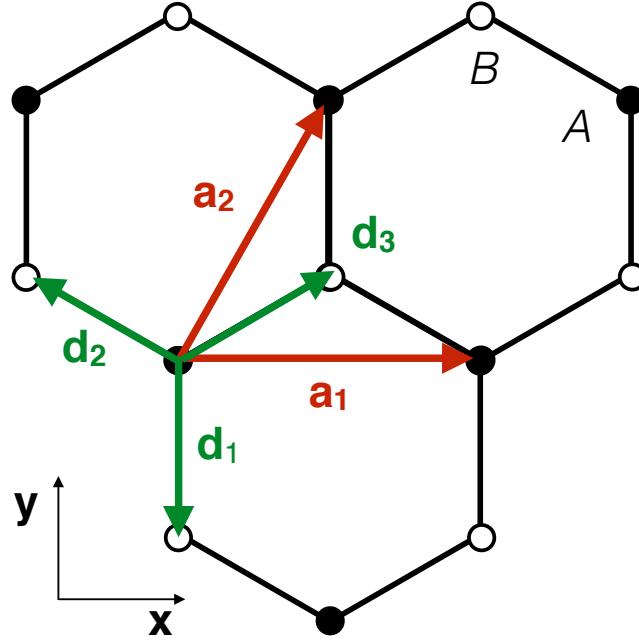


Figure 5.1: Crystal system used for the tight-binding model of BBL heterostructure.

5.1 Crystal system

We consider a buckled honeycomb lattice consists of upper A sublattice and lower B sublattice as shown in Fig. 5.1 We define primitive vectors for direct lattice as

$$\begin{aligned} \mathbf{a}_1 &= a(1, 0) \\ \mathbf{a}_2 &= a\left(\frac{1}{2}, \frac{\sqrt{3}}{2}\right), \end{aligned} \tag{5.1}$$

and primitive vectors for reciprocal lattice are

$$\begin{aligned}\mathbf{b}_1 &= \frac{2\pi}{a} \left(1, -\frac{\sqrt{3}}{3} \right) \\ \mathbf{b}_2 &= \frac{2\pi}{a} \left(0, \frac{2\sqrt{3}}{3} \right).\end{aligned}\tag{5.2}$$

K and K' points in the Brillouin zone are defined as

$$\begin{aligned}K &= \frac{2}{3}\mathbf{b}_1 + \frac{1}{3}\mathbf{b}_2 = \left(\frac{4\pi}{3a}, 0 \right) \\ K' &= -K.\end{aligned}\tag{5.3}$$

And three vectors from a site in A sublattice to three nearest-neighbor (NN) sites in B sublattice are

$$\begin{aligned}\mathbf{d}_1 &= a \left(0, -\frac{1}{\sqrt{3}}, \frac{\cot \theta}{\sqrt{3}} \right) \\ \mathbf{d}_2 &= a \left(-\frac{1}{2}, \frac{1}{2\sqrt{3}}, \frac{\cot \theta}{\sqrt{3}} \right) \\ \mathbf{d}_3 &= a \left(\frac{1}{2}, \frac{1}{2\sqrt{3}}, \frac{\cot \theta}{\sqrt{3}} \right).\end{aligned}\tag{5.4}$$

For a perfect cubic lattice we have $\cot \theta = -\frac{1}{\sqrt{2}}$. Note that we choose the upper sublattice as A sublattice and lower sublattice as B sublattice. For a moment, we restrict our formulation in the case of a perfect cubic. And at the end of the chapter, we will provide the result for a general angle θ .

5.2 Tight-binding hopping Hamiltonian

We are interested in low-energy electronic structure of BBL that is mostly composed of Bi 6s. Also, we are to investigate the origin of the effective SOC in Bi 6s band. For this purpose, we include the Bi 6p orbitals in a basis set. The basis set we choose contains 8 atomic orbitals

$$\{s^A, p_x^A, p_y^A, p_z^A, s^B, p_x^B, p_y^B, p_z^B\}, \quad (5.5)$$

where the superscript A, B is the sublattice index. We set Bi-6s orbital energy as zero energy. Thus the Bi-6p energy E_p is equal to the energy difference between Bi-6p and Bi-6s orbitals.

The general tight-binding hopping matrix is given by

$$H_{\text{hop}}(\mathbf{k}) = \sum_{\mathbf{R}} e^{i\mathbf{k}\cdot(\mathbf{R}+\mathbf{r}_j-\mathbf{r}_i)} \langle i, \mathbf{0} + \mathbf{r}_i | \hat{H} | j, \mathbf{R} + \mathbf{r}_j \rangle, \quad (5.6)$$

where the sum is over the Bravais lattice \mathbf{R} . In this study, we only consider NN hoppings.

For $\mathbf{R} + \mathbf{r}_j - \mathbf{r}_i =$ a NN vector,

$$\langle i, \mathbf{0} + \mathbf{r}_i | \hat{H} | j, \mathbf{R} + \mathbf{r}_j \rangle = E_{ij}(l, m, n) \quad (5.7)$$

where (l, m, n) is a direction cosine of the NN vector. $E_{ij}(l, m, n)$ is the two-center approximation expressed by the direction cosine and four parameters, $V_{ss\sigma}$, $V_{sp\sigma}$, $V_{pp\sigma}$, and $V_{pp\pi}$. Expressions for $E_{ij}(l, m, n)$ are tabulated in Table 5.1. Other terms can be obtained by permuting the indices.

Table 5.1: The energy integral in terms of two-center integrals.

$E_{s,s}$	$V_{ss\sigma}$
E_{s,p_x}	$lV_{sp\sigma}$
E_{p_x,p_x}	$l^2V_{pp\sigma} + (1 - l^2)V_{pp\pi}$
E_{p_x,p_y}	$lmV_{pp\sigma} - lmV_{pp\pi}$
E_{p_z,p_z}	$lnV_{pp\sigma} - lnV_{pp\pi}$

We present the hopping Hamiltonian at the K point explicitly

$$H_{\text{hop}}(K) = \begin{pmatrix} 0 & 0 & 0 & 0 & 0 & \frac{\sqrt{6}i}{2}V_{sp\sigma} & -\frac{\sqrt{6}}{2}V_{sp\sigma} & 0 \\ E_p & 0 & 0 & -\frac{\sqrt{6}i}{2}V_{sp\sigma} & \frac{1}{2}V' & -\frac{i}{2}V' & \frac{\sqrt{2}i}{2}V' \\ E_p & 0 & \frac{\sqrt{6}}{2}V_{sp\sigma} & -\frac{i}{2}V' & -\frac{1}{2}V' & -\frac{\sqrt{2}}{2}V' \\ & E_p & 0 & \frac{\sqrt{2}i}{2}V' & -\frac{\sqrt{2}}{2}V' & 0 \\ & & 0 & 0 & 0 & 0 \\ & & & E_p & 0 & 0 \\ & & & & E_p & 0 \\ & & & & & E_p \end{pmatrix}, \quad (5.8)$$

where $V' = V_{pp\pi} - V_{pp\sigma}$. The lower left part is obtained using the hermiticity of the Hamiltonian.

5.3 Tight-binding SOC Hamiltonian

Spin-orbit coupling matrix among p orbitals is

$$H_{\text{SOC}}^{l=1} = \frac{\lambda}{2} \begin{pmatrix} & |p_x\rangle & |p_y\rangle & |p_z\rangle \\ \hline \langle p_x| & 0 & -i\sigma_z & i\sigma_y \\ \langle p_y| & i\sigma_z & 0 & -i\sigma_x \\ \langle p_z| & -i\sigma_y & i\sigma_x & 0 \end{pmatrix}. \quad (5.9)$$

We include only the on-site SOC in the tight-binding Hamiltonian because its effect is largest near the atomic centers. The tight-binding SOC Hamiltonians is

$$H_{\text{SOC}} = \begin{pmatrix} O_{2 \times 2} & & & \\ & H_{\text{SOC}}^{l=1} & & \\ & & O_{2 \times 2} & \\ & & & H_{\text{SOC}}^{l=1} \end{pmatrix}, \quad (5.10)$$

where $O_{2 \times 2}$ is the 2×2 zero matrix representing the atomic SOC in s -orbital. Other terms that are not written in the above equation are zero.

Including the SOC, the basis set is doubled by

$$\{s^A, p_x^A, p_y^A, p_z^A, s^B, p_x^B, p_y^B, p_z^B\} \otimes \{\uparrow, \downarrow\}. \quad (5.11)$$

The hopping Hamiltonian does not depend on the spin, so that in the new basis it is just doubled. We obtain 16×16 tight-binding Hamiltonian including the spin degree of freedom.

$$H(\mathbf{k}) = H_{\text{hop}}(\mathbf{k}) \otimes I_{2 \times 2} + H_{\text{SOC}}. \quad (5.12)$$

We re-arrange the Hamiltonian in the following form in basis set $\{s^A, s^B, p_{x,y,z}^A, p_{x,y,z}^B\} \otimes \{\uparrow, \downarrow\}$

$$H(\mathbf{k}) = \begin{pmatrix} H_s & H_n \\ H_n^\dagger & H_p \end{pmatrix}, \quad (5.13)$$

where H_s is the 4×4 matrix for s orbitals, H_p is the 12×12 matrix for p orbitals, and H_n is the 4×16 matrix connecting the s and p orbitals.

5.4 Effective low-energy Hamiltonian

We have obtained the 16×16 Hamiltonian describing the BBL heterostructure Eq. 5.13. We could directly solve the Hamiltonian and obtain energy eigenvalues and eigenvectors. Here we take a different approach. Instead, we derive the effective Hamiltonian describing the low-energy band structure of BBL heterostructure. By doing this, we are able to gain more physical insight about the system

We are interested in the following situations: (i) the eigenvalues of H_s are around energy ε while the eigenvalues of H_p are distant from ε . (ii) the energy scale of the non-diagonal block H_n is smaller than the eigenvalue difference

between H_s and H_p . All above conditions are satisfied for our Hamiltonian Eq. 5.13. The effective Hamiltonian around ε can be obtained by the following method. Here, we set $\varepsilon = 0$ because we are interested in the effective Hamiltonian for s -band. We write [SW66]

$$\mathcal{H} = \mathcal{H}_0 + \mathcal{H}_n, \quad (5.14)$$

where

$$\mathcal{H}_0 = \begin{pmatrix} H_s & 0 \\ 0 & H_p \end{pmatrix}, \quad \mathcal{H}_n = \begin{pmatrix} 0 & H_n \\ H_n^* & 0 \end{pmatrix}. \quad (5.15)$$

We perform a canonical transformation

$$\mathcal{H} \rightarrow H_{eff} = e^{-S} \mathcal{H} e^S, \quad (5.16)$$

where

$$S = \begin{pmatrix} 0 & M \\ -M^* & 0 \end{pmatrix}. \quad (5.17)$$

The matrix M can be determined by the condition

$$[\mathcal{H}_0, S] + \mathcal{H}_n = 0. \quad (5.18)$$

After some algebra, we have

$$H_s M - M H_p + H_n = 0. \quad (5.19)$$

The above equation can be solved recursively, and M can be written approximately as

$$M \simeq H_n H_p^{-1}. \quad (5.20)$$

Thus, the effective Hamiltonian has the following form

$$\begin{aligned} H_{eff} &= e^{-S} \mathcal{H} e^S = \mathcal{H} + [\mathcal{H}, S] + \dots \\ &= \mathcal{H}_0 + \frac{1}{2} [\mathcal{H}_n, S] + \dots \end{aligned} \quad (5.21)$$

Finally, up to the second order, we have

$$H_{eff} = H_s - H_n H_p^{-1} H_n^\dagger \quad (5.22)$$

It can be also written in the following form.

$$H_{eff} = PHP + PHQ \frac{1}{QHQ} QHP, \quad (5.23)$$

where P is the projection operator onto the s -orbital subspace and $Q = 1 - P$.

After some algebra we obtained the effective Hamiltonian at the K point in the basis of $\{s^A \uparrow, s^A \downarrow, s^B \uparrow, s^B \downarrow\}$

$$H_{eff}(K) = \begin{pmatrix} -\lambda_{SO} & 0 & 0 & 0 \\ 0 & \lambda_{SO} & 0 & 0 \\ 0 & 0 & \lambda_{SO} & 0 \\ 0 & 0 & 0 & -\lambda_{SO} \end{pmatrix} \quad (5.24)$$

where $\lambda_{SO} = \frac{3V_{sp\sigma}^2}{2E_p^2}\lambda$. Note that without the SOC we end up with zero bandgap at the K . The origin of the band gap is SOC, and band gap is $2\lambda_{SO}$. For BBL system, we have $E_p \sim 10$ eV, $\lambda \sim 1.2$ eV, and typical value of $V_{sp\sigma}$ is around few eV, as a result, the large SOC is possible even for the s -orbital band.

Expanding the Hamiltonian to the linear order in \mathbf{k} around the K point, we obtain

$$H_{eff}^K = \begin{pmatrix} -\lambda_{SO} & a\lambda_R(ik_x + k_y) & \hbar v(k_x + ik_y) & 0 \\ a\lambda_R(-ik_x + k_y) & \lambda_{SO} & 0 & \hbar v(k_x + ik_y) \\ \hbar v(k_x - ik_y) & 0 & \lambda_{SO} & -a\lambda_R(ik_x + k_y) \\ 0 & \hbar v(k_x - ik_y) & -a\lambda_R(-ik_x + k_y) & -\lambda_{SO} \end{pmatrix} \quad (5.25)$$

where $v = -\frac{a\sqrt{3}V_{ss\sigma}}{2\hbar}$, $\lambda_{SO} = \frac{3V_{sp\sigma}^2}{2E_p^2}\lambda$, and $\lambda_R = \frac{\sqrt{6}V_{sp\sigma}^2}{4E_p^2}\lambda$. Note that the a is the nearest distance between Bi atoms in the same sublattice. It is related to the cubic lattice constant, a_c , which is the same as the NN distance by, $a = \sqrt{2}a_c$. And the NN distance projected on the (111) plane, a_p , is, $a_p = \frac{1}{\sqrt{3}}a = \sqrt{\frac{2}{3}}a_c$. Using the Pauli matrices, the above equation can be casted into

$$H_{eff}^\eta = \hbar v(\eta k_x \tau_x - k_y \tau_y) \otimes \sigma_0 - \lambda_{SO} \eta \tau_z \otimes \sigma_z - a\lambda_R \tau_z \otimes (k_x \sigma_y - k_y \sigma_x), \quad (5.26)$$

where $\eta = +1, -1$ for valleys K and K' , σ_i is the Pauli matrix for real spin, and τ_i is the Pauli matrix for sublattice pseudo-spin. Note the valley dependence of each term. The Rashba SOC term is independent of valley index. Also note that

if we re-label the A sublattice as B sublattice and vice versa, the $\boldsymbol{\tau}$ transforms as $\tau_x \rightarrow \tau_x$, $\tau_y \rightarrow -\tau_y$, $\tau_z \rightarrow -\tau_z$. (cf. equations in Chapters 3 and 4)

Next we include the sublattice energy difference, Δ , in the following form in the basis set $\{s^A, p_x^A, p_y^A, p_z^A, s^B, p_x^B, p_y^B, p_z^B\} \otimes \{\uparrow, \downarrow\}$.

$$H_\Delta = \begin{pmatrix} \frac{\Delta}{2} I_{4 \times 4} & 0 \\ 0 & -\frac{\Delta}{2} I_{4 \times 4} \end{pmatrix} \otimes \sigma_0. \quad (5.27)$$

The total tight-binding Hamiltonian is

$$H(\mathbf{k}) = H_{\text{hop}}(\mathbf{k}) \otimes I_{2 \times 2} + H_{\text{SOC}} + H_\Delta. \quad (5.28)$$

By the same way, we can obtain the effective Hamiltonian. The result is

$$H_K^{\text{eff}} = \begin{pmatrix} \frac{\Delta}{2} - \lambda_{SO}^A & a\lambda_R^A(ik_x + k_y) & \hbar v(k_x + ik_y) & 0 \\ a\lambda_R^A(-ik_x + k_y) & \frac{\Delta}{2} + \lambda_{SO}^A & 0 & \hbar v(k_x + ik_y) \\ \hbar v(k_x - ik_y) & 0 & -\frac{\Delta}{2} + \lambda_{SO}^B & -a\lambda_R^B(ik_x + k_y) \\ 0 & \hbar v(k_x - ik_y) & -a\lambda_R^B(-ik_x + k_y) & -\frac{\Delta}{2} - \lambda_{SO}^B \end{pmatrix}, \quad (5.29)$$

where $\lambda_{SO}^A = \lambda_{SO} \frac{E_p^2}{(E_p - \Delta)^2}$, $\lambda_R^A = \lambda_R \frac{E_p^2}{(E_p - \Delta)^2}$, $\lambda_{SO}^B = \lambda_{SO} \frac{E_p^2}{(E_p + \Delta)^2}$, and $\lambda_R^B =$

$\lambda_R \frac{E_p^2}{(E_p + \Delta)^2}$. And it can be re-written by using the Pauli matrices.

$$\begin{aligned}
H_{eff}^\eta &= \hbar v (\eta k_x \tau_x - k_y \tau_y) \otimes \sigma_0 + \frac{\Delta}{2} \tau_z \otimes \sigma_0 \\
&- \lambda_{SO}^A \eta \frac{\tau_z + \tau_0}{2} \otimes \sigma_z - \lambda_{SO}^B \eta \frac{\tau_z - \tau_0}{2} \otimes \sigma_z \\
&- a \lambda_R^A \frac{\tau_z + \tau_0}{2} \otimes (k_x \sigma_y - k_y \sigma_x) - a \lambda_R^B \frac{\tau_z - \tau_0}{2} \otimes (k_x \sigma_y - k_y \sigma_x).
\end{aligned} \tag{5.30}$$

Note that in this case A , B sublattices feel the different size of SOC, so that different size of spin splitting occur.

Up to now, we restrict our theory for a perfect cubic lattice. Here, we present results for a general angle. The calculation process is similar. From the obtained low-energy effective Hamiltonian in momentum space, NNN hopping process in real space can be obtained. The effective NNN hopping is written as

$$\begin{aligned}
H_{NNN} &= -i \frac{\lambda_{SO}}{3\sqrt{3}} \frac{3}{2(1 + \cot^2 \theta)} \sum_{\langle\langle i,j \rangle\rangle_{\alpha\beta}} \nu_{ij} c_{i\alpha}^\dagger \sigma_z^{\alpha\beta} c_{j\beta} \\
&- i \frac{2\lambda_{SO}}{3} \frac{-3\sqrt{2} \cot \theta}{\sqrt{6} 2(1 + \cot^2 \theta)} \sum_{\langle\langle i,j \rangle\rangle_{\alpha\beta}} \mu_{ij} c_{i\alpha}^\dagger (\boldsymbol{\sigma} \times \mathbf{d}_{ij})_z^{\alpha\beta} c_{j\beta},
\end{aligned} \tag{5.31}$$

where the first term was explained in Chapter 2. It is the spin-conserving NNN hopping responsible for the non-trivial mass and turns the system to the QSH insulator. The second part is the intrinsic Rashba SOC arising from the buckled structure. It results in a Rashba-like in-plane spin texture around K and K' . We comment on the angle dependence. The first term gets larger as the structure becomes planar while the second term gets smaller and vanishes at $\theta = \pi/2$. This behavior is different from that observed in a p_z -orbital

system, where the SOC gap is increasing with buckling angle.

Chapter 6

Discussion

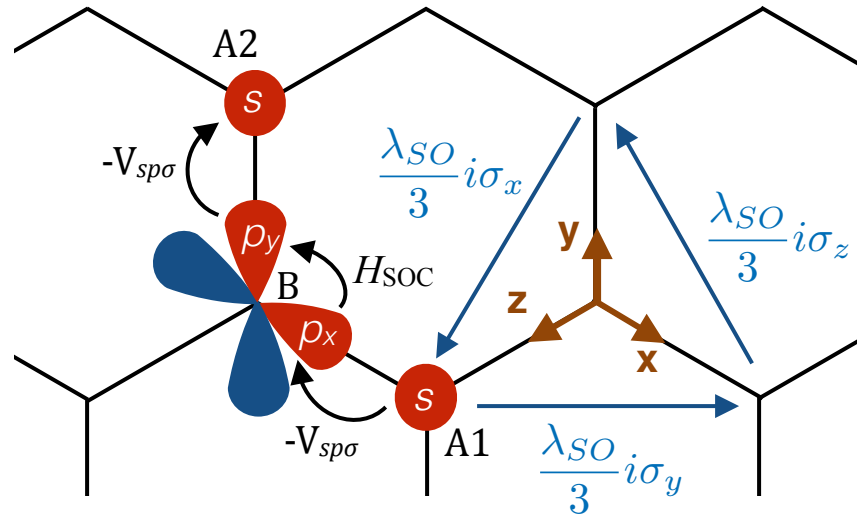
In this chapter, we discuss the results. We give a simple description of SOC process in BBL heterostructure. Also, we touch on the issue of charge-ordering instability at symmetric configuration.

6.1 Spin-orbit coupling in s -orbital Dirac cone

The large SOC is crucial in both QSH and QVH phases when aiming at spintronics and valleytronics applications. We observe that the BBL heterostructure, even with its s -orbital character, provide the substantial SOC. The SOC in BBL heterostructures is due to the s - p hybridization and the large atomic SOC strength of Bi-6p orbitals. The Bi-6s orbital can hybridize with the nearest-neighbor (NN) Bi-6p orbital, and the effective complex-valued hopping between next-NN (NNN) Bi-6s orbitals can be induced through the large SOC in Bi-6p orbitals.

Specific process for a hopping channel is illustrated in Fig. 6.1, in which the local xyz axis is used to represent p orbitals and eigenstates of s_z . The NNN interaction involves three hoppings: (i) hopping from $s^{A1} \otimes \beta$ to $p_x^B \otimes \beta$ with amplitude of $-V_{sp\sigma}$, (ii) SOC that turns the $p_x^B \otimes \beta$ to $p_y^B \otimes \alpha$ expressed by $\frac{\lambda}{2}i\sigma_z^{\alpha\beta}$, and (iii) hopping from $p_y^B \otimes \alpha$ to $s^{A2} \otimes \alpha$ with $V_{sp\sigma}$. Here, $V_{sp\sigma}$ is the Slater-Koster hopping parameter, and α, β represents spin states. Overall, the effective NNN hopping from $s^{A1} \otimes \beta$ to $s^{A2} \otimes \alpha$ is given by $\frac{\lambda_{SO}}{3}i\sigma_z^{\alpha\beta}$, where $\lambda_{SO} = \frac{2V_{sp\sigma}^2}{E_p}$, with E_p being the Bi 6p-orbital energy relative to the Bi 6s-orbital one. NNN hoppings for other directions are easily obtained and shown in Fig. 6.1. With DFT calculations, we obtained $E_p \sim 10$ eV, $\lambda \sim 1.2$ eV, and typical value of $V_{sp\sigma}$ is around few eV, as a result, the large SOC is possible even for the s -orbital band. The concise description of SOC and its large size is the distinctive feature of s -orbital Dirac cone in BBL heterostructure.

The above process might seems similar to that observed in silicene, where the Si p_z orbitals (with respect to [111] direction) are composing the Dirac



$$H_{\text{SOC}} = \frac{\lambda}{2} \begin{pmatrix} & |p_x\rangle & |p_y\rangle & |p_z\rangle \\ \langle p_x| & 0 & -i\sigma_z & i\sigma_y \\ \langle p_y| & i\sigma_z & 0 & -i\sigma_x \\ \langle p_z| & -i\sigma_y & i\sigma_x & 0 \end{pmatrix}$$

Figure 6.1: The next-nearest-neighbor hopping process is illustrated. See the text for a detailed description.

cone and the SOC is allowed by hybridization of p_z and $p_{x,y}$ orbitals in buckled structure [LJY11]. But compared to the silicene, the hopping from Bi-6s to Bi 6 $p_{x,y}$ is possible even without the buckling in BBL. In fact, as the buckling angle get closer to of the planar structure, the SOC become lager in BBL, which is completely different from p_z -orbital Dirac cone system.

Moreover, when the sublattice energy difference of is introduced by SIA or BIA (assuming that the sublattice A has higher energy then the sublattice B by Δ), the sublattice A feels the SOC of $\lambda_{SO}^A = \frac{3V_{sp\sigma}^2}{2(E_p - \Delta)^2} \lambda$, while the sublattice B experiences $\lambda_{SO}^B = \frac{3V_{sp\sigma}^2}{2(E_p + \Delta)^2} \lambda$. This is because the SOC process described above involves, in fact, the energy difference between Bi 6s in one sublattice and Bi 6p in the other sublattice. This effect is clearly manifested in different spin splitting in conduction and valence bands as shown in Fig. 4.5(a).

6.2 Charge-ordering instability at symmetric configuration

The bulk BBO is known to crystalize in a monoclinic lattice with the charge-ordering of Bi³⁺ and Bi⁵⁺ accompanied by breathing instability [CS76]. The charge state of Bi in BBL is related to the firmness of QSH phase in symmetric configuration because the charge-ordering gap, which is trivial, could compete with the non-trivial gap by SOC. To verify whether the charge-ordering instability is present in the symmetric configuration, we applied an electric field along the [111] direction to the slab geometry of BaZrO₃/BBL/BaZrO₃ and examine the bandgap and charge states of Bi. As shown in Fig. 6.2, the bandgap

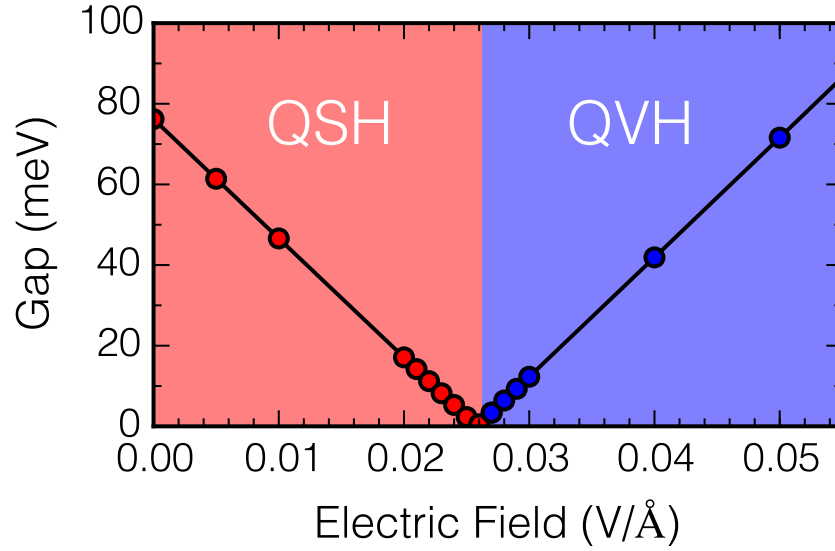


Figure 6.2: The relation between the bandgap and the external electric field.

is linearly decreasing with the bandgap closing at $26 \text{ V}/\text{\AA}$, and bandgap re-opens and linearly increase with electric field. In the investigated electric field range, we do not observe an abrupt jump of bandgap that would present if the charge ordering instability set in. This suggests that the BBL in the symmetric configuration is stable against the charge ordering instability, and therefore the QSH phase is not disturbed.

Chapter 7

Summary and perspective

In this thesis, in an attempt to search the practical candidates for topological electronics, we suggested the (111)-oriented BaBiO₃-bilayer (BBL) sandwiched by large gap perovskite oxides, which is denoted by BaXO₃/BBL/BaYO₃. We carried out first-principles calculations for various symmetric and asymmetric configurations.

To understand this system, we first studied in detail the general physics of honeycomb system. Tight-binding model that describe the graphene and silicene was investigated. It was shown the the general Dirac mass could be introduce and is tunable for the silicene due to its buckled structure, which is also describe the crystal structure BBL heterostructure. Analytic form of general Dirac Hamiltonian for these system were obtained. For this Hamiltonian, Chern number indexed by spin and valley, \mathcal{C}_s^η , were calculated. Chern numbers were shown to quantized by half-integer. Using four Chern numbers, we classified the topological phases in honeycomb system. In particular, quantum spin Hall and quantum valley Hall phases were given special intention.

Turning to the first-principles calculations, when the same materials sandwich the BBL (symmetric configuration), the s -orbital Dirac cone was emerging. The Dirac cone was located within the bandgaps of sandwich layers. Due to the large spin-orbit coupling of the Bi- p orbital, the s -orbital Dirac cone opened a gap at K point through effective next-nearest-neighbor hopping process. This induced the non-trivial gap which turns the system into the QSH phase. Especially, for the BaZrO₃/BBL/BaZrO₃, the gap size was 79 meV, which is enough to be observed in room temperature. Various sandwich materials (BaTiO₃, BaZrO₃, BaSnO₃, BaHfO₃, and BaCeO₃) all gave substantial non-trivial gaps. It was also shown that the Sr-based system can be understood by the same physics.

For an asymmetric configuration, in which the top and bottom layers are different, QVH phase was arised. The QVH phase was a result of the inversion symmetry breaking induced by structural inversion asymmetry of different top and bottem layers. For QVH phase, spin and valley was shown to be coupled. The spin-texture at K and K' were exactly opposite becaus they were only connected by time-reversal symmetry. In addition, due to the buckled structure of BBL, intrinsic Rashba SOC result in in- and out-of-plane spin textures.

We also suggested a ferroelectric control of topological phases in BaTiO₃/BBL/BaTiO₃ heterostructure, where the QSH and QVH phases could be controlled via switching the polarization directions of BaTiO₃ layer. The (111) BBL heterostructure was proposed to be a unified feasible platform for spintronics and valleytronics as well as for topological engineering of the two-dimensional electron system.

Slater-Koster type tight-binding model that describe the BBL heterostruc-

ture was constructed. The low-energy effective Hamiltonian, which has a form of Dirac Hamiltonian, is obtained from the full tight-binding Hamiltonian. We explained how the SOC is obtained in s -band through the next-nearest-neighbor hopping process. We also discussed the issue of charge-ordering instability at symmetric configuration.

Three research areas in condensed matter physics are involved in the s -orbital Dirac fermion and its various topological phases in the (111) BBL heterostructure. They are Dirac materials, oxide heterostructures, and topological electronics. This system brings the Dirac cone band structure in the oxide system, heterostructures modifies and controls the bandgap at the Dirac point, and at the domain boundary of the system topological edge states could be realized. Taking advantage of these fact, we are able to design the integrated topological electronic devices based on the above ingredients. In addition, if we introduce the magnetic layer to the system, it is expected that the other topological pahses including quantum anomalous Hall phase are realized. Moreover, the multiferroic layer that can control both the inversion symmetry and time-reversal symmetry can be utilized to control the various degrees of freedom in this system. By taking account of the charge, spin, valley, and sublattice degrees of freedom of the Dirac fermion in BBL heterostructre and the various states of the oxide perovskites heterostrucutre we may find a novel play ground of topological quantum matters in this combined research area.

Bibliography

- [CS76] D E Cox and A W Sleight. Crystal structure of $\text{Ba}_2\text{Bi}^{3+}\text{Bi}^{5+}\text{O}_6$. *Solid State Commun.*, 19(10):969–973, August 1976.
- [DSSB⁺15] Domenico Di Sante, Alessandro Stroppa, Paolo Barone, Myung-Hwan Whangbo, and Silvia Picozzi. Emergence of ferroelectricity and spin-valley properties in two-dimensional honeycomb binary compounds. *Phys. Rev. B*, 91(16):161401(R), April 2015.
- [DZF12] N D Drummond, V Zólyomi, and V I Fal’ko. Electrically tunable band gap in silicene. *Phys. Rev. B*, 85(7):075423, February 2012.
- [Eza13] Motohiko Ezawa. Spin valleytronics in silicene: Quantum spin Hall–quantum anomalous Hall insulators and single-valley semimetals. *Phys. Rev. B*, 87(15):155415, April 2013.
- [Eza15] Motohiko Ezawa. Monolayer Topological Insulators: Silicene, Germanene and Stanene. *arXiv.org*, cond-mat.mes-hall:arXiv:1504.08914v1, March 2015.
- [FK06] Liang Fu and C L Kane. Time reversal polarization and a \mathbb{Z}_2 adiabatic spin pump. *Phys. Rev. B*, 74(19):195312, November 2006.

- [FR14] Gregory A Fiete and Andreas Rüegg. Topological Phases in Oxide Heterostructures with Light and Heavy Transition Metal Ions. *arXiv.org*, cond-mat.str-el:arXiv:1409.7148v1, September 2014.
- [GZSÍ12] M Gibert, P Zubko, R Scherwitzl, and J Íñiguez. Exchange bias in LaNiO_3 - LaMnO_3 superlattices. *Nat. Mater.*, 11(3):195, 2012.
- [Hal88] F D M Haldane. Model for a Quantum Hall Effect without Landau Levels: Condensed-Matter Realization of the "Parity Anomaly". *Phys. Rev. Lett.*, 61(18):2015, October 1988.
- [HK64] P Hohenberg and W Kohn. Inhomogeneous Electron Gas. *Phys. Rev.*, 136(3B):B864–B871, November 1964.
- [HK10] M Z Hasan and C L Kane. Colloquium: Topological insulators. *Rev. Mod. Phys.*, 82(4):3045, November 2010.
- [HMT15] Daigorou Hirai, Jobu Matsuno, and Hidenori Takagi. Fabrication of (111)-oriented $\text{Ca}_{0.5}\text{Sr}_{0.5}\text{IrO}_3/\text{SrTiO}_3$ superlattices—A designed playground for honeycomb physics. *APL Mater.*, 3(4):041508, April 2015.
- [KF96a] Georg Kresse and J. Furthmüller. Efficiency of ab-initio total energy calculations for metals and semiconductors using a plane-wave basis set. *Comp. Mater. Sci.*, 6(1):15, 1996.
- [KF96b] Georg Kresse and J. Furthmüller. Efficient iterative schemes for ab initio total-energy calculations using a plane-wave basis set. *Phys. Rev. B*, 54(16):11169, 1996.

- [KLB93] G H Kwei, A C Lawson, and S. J. L. Billinge. Structures of the ferroelectric phases of barium titanate. *J. Phys. Chem.*, 97(10):2368–2377, 1993.
- [KM05] C L Kane and E J Mele. Z_2 Topological Order and the Quantum Spin Hall Effect. *Phys. Rev. Lett.*, 95(14):146802, September 2005.
- [LFY11] Cheng-Cheng Liu, Wanxiang Feng, and Yugui Yao. Quantum Spin Hall Effect in Silicene and Two-Dimensional Germanium. *Phys. Rev. Lett.*, 107(7):076802, August 2011.
- [LJY11] Cheng-Cheng Liu, Hua Jiang, and Yugui Yao. Low-energy effective Hamiltonian involving spin-orbit coupling in silicene and two-dimensional germanium and tin. *Phys. Rev. B*, 84(19):195430, November 2011.
- [LKC⁺14] Xiaoran Liu, M Kareev, Yanwei Cao, Jian Liu, S Middey, D Meyers, J W Freeland, and J Chakhalian. Electronic and magnetic properties of (111)-oriented CoCr_2O_4 epitaxial thin film. *Appl. Phys. Lett.*, 105(4):042401, July 2014.
- [LMBM10] Jian Li, Alberto F Morpurgo, Markus Büttiker, and Ivar Martin. Marginality of bulk-edge correspondence for single-valley Hamiltonians. *Phys. Rev. B*, 82(24):245404, December 2010.
- [LWH13] Qi-Feng Liang, Long-Hua Wu, and Xiao Hu. Electrically tunable topological state in [111] perovskite materials with an antiferromagnetic exchange field. *New J. Phys.*, 15(6):063031, June 2013.

- [MB68] Shang-Keng Ma and Keith A Brueckner. Correlation Energy of an Electron Gas with a Slowly Varying High Density. *Phys. Rev.*, 165(1):18–31, January 1968.
- [MMD⁺14] S Middey, D Meyers, D Doennig, M Kareev, X Liu, Y Cao, P J Ryan, R Pentcheva, J W Freeland, and J Chakhalian. Geometrically engineered Mott phases in (111) oriented nickelate superlattices. *arXiv.org*, cond-mat.str-el:arXiv:1407.1570v2, July 2014.
- [MMK⁺12] S Middey, D Meyers, M Kareev, E J Moon, B A Gray, X Liu, J W Freeland, and J Chakhalian. Epitaxial growth of (111)-oriented LaAlO₃/LaNiO₃ ultra-thin superlattices. *Appl. Phys. Lett.*, 101(26):261602, 2012.
- [MV97] Nicola Marzari and David Vanderbilt. Maximally-localized generalized Wannier functions for composite energy bands. *Phys. Rev. B*, 56(12):12847–12865, July 1997.
- [MYL⁺08] Arash A Mostofi, Jonathan R Yates, Young-Su Lee, Ivo Souza, David Vanderbilt, and Nicola Marzari. wannier90: A tool for obtaining maximally-localised Wannier functions. *Comput. Phys. Commun.*, 178(9):685, May 2008.
- [NLT⁺11] Zeyuan Ni, Qihang Liu, Kechao Tang, Jiaxin Zheng, Jing Zhou, Rui Qin, Zhengxiang Gao, Dapeng Yu, and Jing Lu. Tunable Bandgap in Silicene and Germanene. *Nano Lett.*, 12(1):113, December 2011.

- [OZN⁺14] Satoshi Okamoto, Wenguang Zhu, Yusuke Nomura, Ryotaro Arita, Di Xiao, and Naoto Nagaosa. Correlation effects in (111) bilayers of perovskite transition-metal oxides. *Phys. Rev. B*, 89(19):195121, May 2014.
- [PBE96] John P Perdew, Kieron Burke, and Matthias Ernzerhof. Generalized Gradient Approximation Made Simple. *Phys. Rev. Lett.*, 77(18):3865–3868, October 1996.
- [Pro09] Emil Prodan. Robustness of the spin-Chern number. *Phys. Rev. B*, 80(12):125327, September 2009.
- [PW92] John P Perdew and Yue Wang. Accurate and simple analytic representation of the electron-gas correlation energy. *Phys. Rev. B*, 45(23):13244–13249, June 1992.
- [QJL⁺12] Zhenhua Qiao, Hua Jiang, Xiao Li, Yugui Yao, and Qian Niu. Microscopic theory of quantum anomalous Hall effect in graphene. *Phys. Rev. B*, 85(11):115439, March 2012.
- [QZ11] Xiao-Liang Qi and Shou-Cheng Zhang. Topological insulators and superconductors. *Rev. Mod. Phys.*, 83(4):1057, October 2011.
- [SK54] John C Slater and George F Koster. Simplified LCAO method for the periodic potential problem. *Phys. Rev.*, 94(6):1498, 1954.
- [SMV01] Ivo Souza, Nicola Marzari, and David Vanderbilt. Maximally localized Wannier functions for entangled energy bands. *Phys. Rev. B*, 65(3):035109, December 2001.

- [SW66] J R Schrieffer and P A Wolff. Relation between the Anderson and Kondo Hamiltonians. *Phys. Rev.*, 149(2):491, September 1966.
- [SWSH06] D N Sheng, Z Y Weng, L Sheng, and F D M Haldane. Quantum Spin-Hall Effect and Topologically Invariant Chern Numbers. *Phys. Rev. Lett.*, 97(3):036808, July 2006.
- [TQY⁺11] Wang-Kong Tse, Zhenhua Qiao, Yugui Yao, A H MacDonald, and Qian Niu. Quantum anomalous Hall effect in single-layer and bilayer graphene. *Phys. Rev. B*, 83(15):155447, April 2011.
- [XLF⁺12] Di Xiao, Gui-Bin Liu, Wanxiang Feng, Xiaodong Xu, and Wang Yao. Coupled Spin and Valley Physics in Monolayers of MoS₂ and Other Group-VI Dichalcogenides. *Phys. Rev. Lett.*, 108(19):196802, May 2012.
- [XYN07] D Xiao, W Yao, and Q Niu. Valley-contrasting physics in graphene: Magnetic moment and topological transport. *Phys. Rev. Lett.*, 99(23):236809, 2007.
- [XYZ⁺13] Yong Xu, Binghai Yan, Hai-Jun Zhang, Jing Wang, Gang Xu, Peizhe Tang, Wenhui Duan, and Shou-Cheng Zhang. Large-Gap Quantum Spin Hall Insulators in Tin Films. *Phys. Rev. Lett.*, 111(13):136804, September 2013.
- [XZR⁺11] D Xiao, W Zhu, Y Ran, N Nagaosa, and Satoshi Okamoto. Interface engineering of quantum Hall effects in digital transition metal oxide heterostructures. *Nat. Commun.*, 2:596, 2011.

- [YBS⁺15] Kunihiko Yamauchi, Paolo Barone, Tatsuya Shishidou, Tamio Oguchi, and Silvia Picozzi. Coupling Ferroelectricity with Spin-Valley Physics in Oxide-Based Heterostructures. *Phys. Rev. Lett.*, 115(3):037602, 2015.
- [YXS⁺11] Yunyou Yang, Zhong Xu, L Sheng, Baigeng Wang, D Y Xing, and D N Sheng. Time-Reversal-Symmetry-Broken Quantum Spin Hall Effect. *Phys. Rev. Lett.*, 107(6):066602, August 2011.
- [ZJF⁺11] Fan Zhang, Jeil Jung, Gregory A Fiete, Qian Niu, and Allan H MacDonald. Spontaneous Quantum Hall States in Chirally Stacked Few-Layer Graphene Systems. *Phys. Rev. Lett.*, 106(15):156801, April 2011.
- [ZLL⁺14] Xiuwen Zhang, Qihang Liu, Jun-Wei Luo, Arthur J Freeman, and Alex Zunger. Hidden spin polarization in inversion-symmetric bulk crystals. *Nat. Phys.*, 10(5):387, April 2014.
- [ZMM13] Fan Zhang, Allan H MacDonald, and Eugene J Mele. Valley Chern numbers and boundary modes in gapped bilayer graphene. *PNAS*, 110(26):10546, June 2013.

국문 초록

낮은 에너지 전자들이 무질량 디랙 페르미온으로 기술되는 대표적인 이차원계 물질인 그래핀은 사람들의 큰 관심을 끌고 있고, 이차원 물질 연구가 급격히 증가하는 시발점이 되었다. 이 물질의 다양한 응용 가운데, 그래핀은 위상학적 전자공학의 플랫폼으로 제안되었다. Kane 과 Mele 이 그래핀에서의 양자 스핀 홀 효과를 예측한데 이어서, 디랙 포인트에서 띠틈을 조절함으로써 다양한 위상학적 상이 구현됨이 밝혀졌다. 예를들어 스핀-궤도 작용으로 띠틈이 열리면 양자 스핀 홀 상이 구현되고, 반전 대칭을 깨므로써 양자 벨리 홀 상이 나오게 된다. 또한 시간 되집기 대칭을 깨면 양자 비정상 홀 상도 구현될 수 있다. 위상학적 전자공학으로 잘 응용되기 위해서는 큰 스핀-궤도 작용과 쉬운 띠틈 조절이 필요하지만, 이것은 그래핀에선 실현되기가 어렵다.

위상학적 전자공학의 유용한 물질을 찾고자 노력의 일환으로, 우리는 (111)-방향 BaBiO_3 -겹층이 큰 띠틈을 가지는 페롭스카이트 산화물로 위아래로 쌓여진 구조가 위상학적 전자공학의 이상적인 플랫폼이 될 것으로 제안한다. 낮은 에너지 전자구조는 별집 격자 위의 s 궤도 함수로 기술이되고, 그 결과 s 궤도 함수 디랙 페르미온이 발현된다. 가장 가까운 이웃간의 Bi $6s$ 와 Bi $6p$ 궤도 함수 간의 상호작용으로 s 궤도 함수에서 큰 스핀-궤도 작용이 가능하다. 또한 산화물 이질구조에서 비롯된 다양한 질서 변수들은 디랙 포인트에서의 다양한 띠틈을 열수 있고, 따라서 위상학적 상을 조절할 수 있게 한다.

(111)-방향 BaBiO₃-겹층 이질구조 에서 나오는 *s* 궤도 함수 디락 페르미온과 여기서 구현되는 다양한 위상학적 상은 현재 고체 물리 연구 세가지 분야(디락 물질, 산화물 이질구조, 위상학적 전자공학)의 접점에서 나온다. 이 물질은 그 래핀과 같은 디락 전자구조를 산화물에서 구현하고, 산화물 이질구조를 통해 디락 포인트에서 띠틈을 조절함으로써 다양한 위상학적 상을 구현한다. 벌집 격자 구조가 가지는 전하, 스핀, 벨리, 부분격자 유사스핀의 자유도와 산화물 이질구조의 다양한 질서 변수를 활용하면 BaBiO₃ 겹층 이질구조는 위상체 모듬 연구의 이상적인 출발점이 될 것이다.

주요어: BaBiO₃, 이질 구조, 벌집 격자, 양자 스핀 홀, 양자 벨리 홀

학번: 2008-20420